22

Modeling and Parameter Identification of Electric Machines

Ali Keyhani, Wenzhe Lu, and Bogdan Proca
Ohio State University, Columbus, Ohio

NOMENCLATURE

$\hat{(\cdot)}$	: Estimate of $(\cdot)$
$[\ ]^T$	: Transpose of $[\ ]$
$E[\cdot]$	: The operation of taking the expected value of $[\cdot]$
$w(\cdot)$	: Process noise sequence
$v(\cdot)$	: Measurement noise sequence
$X(\cdot)$	: State vector
$Y(\cdot)$	: Measured output vector in the presence of noise
Q	: Covariance of the process noise sequence
R_0	: Covariance of the measurement noise sequence
$R(\cdot)$	: Covariance of the state vector
$e(\cdot)$	: Estimation error, $e(k) = Y(k) - \hat{Y}(k)$
exp	: The exponential operator
det	: Determinant
$\hat{Y}(k \mid k-1)$	: The estimated value of *Y(k)* at time instant *k* given the data up to *k*-1
$U(\cdot)$	: Input vector
$\theta(\cdot)$	: Parameter vector

22.1 INTRODUCTION

Modeling the dynamical properties of a system is an important step in analysis and design of control systems. Modeling often results in a parametric model of the system which contains several unknown parameters. Experimental data are needed to estimate the unknown parameters.

Electric machines are now widely used in electric/hybrid vehicles. To identify appropriate model structures of these machines and estimate the parameters of the models become an important part of the automotive control design.

Generally, the parameter estimation from test data can be done in frequency-domain or time-domain. Since noise is an inherent part of the test data, which may cause problems to parameters estimation, we will first study the effects of noise on frequency-domain parameter estimation. To examine this issue, we will study the identification of synchronous machine parameters from noise-corrupted measurements. Then, we will show how the time-domain maximum likelihood technique can be used to remove the effect of noise from estimated parameters. The models and the procedures to identify the parameters of synchronous, induction, and switched reluctance machines using experimental data will be presented.

22.2 CASE STUDY: THE EFFECTS OF NOISE ON FREQUENCY-DOMAIN PARAMETER ESTIMATION OF SYNCHRONOUS MACHINE

22.2.1 PROBLEM DESCRIPTION

A solid-rotor machine consists essentially of an infinite number of rotor circuits. However, in practice, only a three-rotor-winding or a two-rotor-winding model is used in estimating machine parameters from test data. Experience gained in modeling of many machines shows that neither the second nor the third order model structure can be an exact mathematical representation of a machine.

In estimating the parameters of a system, one question needs to be answered. If the assumed model structure is correct, then can one obtain a unique estimate of the parameters from noise-corrupted frequency response data? The answer to this question cannot be found from measurements, since the measurements are made on a machine with a complex, high order rotor circuit, with unknown structure and unknown parameters.

If one assumes a model structure and then proceeds with estimating its parameters from actual measurements, then the structural error and the effect of noise in the measurements will result in inaccurate parameters. Therefore, it will not be clear whether the discrepancy between the simulated model response and the measured response is due to the effect of noise on the parameters, inadequacy of the assumed model structure, or both. Therefore, the structural identification problem and the parameter estimation problem should be studied separately. There is a need to show that the measurements noise will not corrupt the estimated parameters when the parameters of an assumed structure are estimated from the frequency response measurements.

In this section, a third order machine model with known parameters is simulated and then the data are noise-corrupted using a known noise distribution. The objective is to estimate the parameters of this model from the noise-corrupted data and evaluate the estimated parameters by comparison with the known parameters.

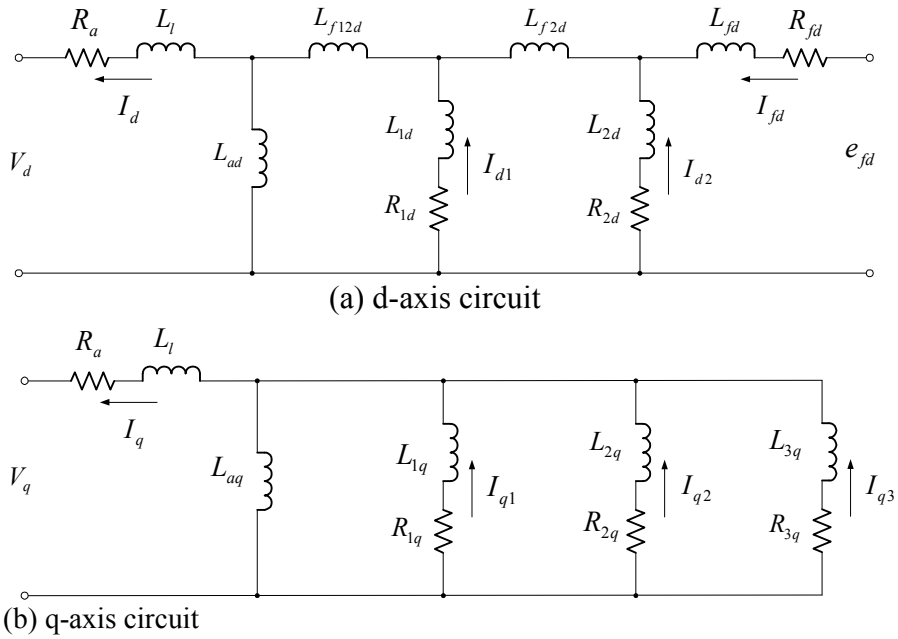

Figure 22.1 SSFR3 Equivalent Circuit Structures

22.2.2 PARAMETERS ESTIMATION TECHNIQUE

In the literature the second order model of synchronous machine is referred to as SSFR2 and the third order model as SSFR3. These notations will be used in this section. It is generally assumed that the synchronous machine d-axis and q-axis circuit structures can be represented by the SSFR3 or the SSFR2 models. The SSFR3 model is shown in Figure 22.1. The SSFR2 model structure can be obtained from the SSFR3 model by reducing the number of rotor body circuits from two to one and also assuming that L_{f2d}, which reflects the leakage flux effect, is zero. The standard circuit model structure can be obtained by assuming that L_{f12d} is also negligible.

23.2.2.1 Estimation of d-axis Parameters from the Time Constants

The transfer functions of the d-axis SSFR3 equivalent circuits are:

$$L_d(s) = K_d \frac{(1+T_1 s)(1+T_2 s)(1+T_3 s)}{(1+T_4 s)(1+T_5 s)(1+T_6 s)} \tag{22.1}$$

$$sG(s) = G_d \frac{(1+T_7 s)(1+T_8 s)}{(1+T_4 s)(1+T_5 s)(1+T_6 s)} \tag{22.2}$$

Using an assumed value of armature resistance, R_a, the $L_d(s)$ is calculated from the operational impedance, $Z_d(s) = -V_d(s) / I_d(s)$, and $sG(s)$ is calculated from $I_{fd}(s) / I_d(s)$ when the field is short-circuited.

The equations which relate the circuit parameters to the time constants can be obtained from Equations 22.1 and Equation 22.2. These equations are described in terms of the

Table 22.1 Definitions for D-Axis Circuit Unknowns and Knows

Unknown Circuit Parameters	Unknown Vector $\bar{x}$	Known Constants	Known Vector $\bar{y}$
L_{ad}	x_1	L_1	y_0
L_{f12d}	x_2	K_d	y_1
R_{1d}	x_3	$T_1T_2T_3$	y_2
L_{1d}	x_4	$T_1T_2 + T_1T_3 + T_2T_3$	y_3
L_{f2d}	x_5	$T_1 + T_2 + T_3$	y_4
R_{2d}	x_6	$T_{41}T_5T_6$	y_5
L_{2d}	x_7	$T_4T_5 + T_4T_6 + T_5T_6$	y_6
R_{fd}	x_8	$T_4 + T_5 + T_6$	y_7
L_{fd}	x_9	G_d	y_8
-		T_7T_8	y_9
-		$T_7 + T_8$	y_{10}

unknown vector $\bar{x}$ (i.e., the circuit parameters) and the known vector $\bar{y}$, as defined in Table 22.1.

The vector $\bar{y}$ is estimated from the measured frequency response data of transfer functions. The time constants are estimated by using a curve-fitting technique described in references [15,16,20]. The functional form of the vector $\bar{y}$ which relates to the circuit parameters (i.e., the vector $\bar{x}$) can be derived using MACSYMA [21], a computer-aided symbolic processor. These relationships are complex and nonlinear, and can be written as:

$$f_i(\bar{x}) = \bar{y}_i + g_i(\bar{x}, \bar{y}) + \zeta_i = 0 \tag{22.3}$$

where $i = 1, \ldots, 10$.

Details of these equations are given in Appendix A. In general, these ten equations are nonlinear in nature and are not consistent with each other. This is due to the noise ζ imbedded in vector $\bar{y}$. Because of the nonlinearity of these equations, a closed form solution for vector $\bar{x}$ may not be possible, and a numerical technique such as Newton-Raphson method may have to be used to solve these equations iteratively. Moreover, these are a redundant set of equations, ten equations with nine unknown parameters. Because of the inconsistency of these equations, multiple solutions will be obtained depending on which equation is ignored.

If the measured frequency response data are noise free (i.e., $\zeta_i = 0$, $i = 1, \ldots, 10$.), then equations A.1 through Equation A.10, given in Appendix A, would be consistent, and a unique solution will be obtained regardless of the equation which is ignored.

The set of nonlinear equations, $F(\bar{x}) = [f_1(\bar{x}), f_2(\bar{x}), \ldots f_{10}(\bar{x})] = 0$, can be solved by updating $\bar{x}$ as:

$$\bar{x}^{K+1} = \bar{x}^K + \Delta\bar{x}^K, \; K = 0, 1, 2 \ldots \tag{22.4}$$

where

$$\Delta \bar{x}^K = -\left[\frac{\partial F}{\partial \bar{x}}\right]^{-1}_{\bar{x}=\bar{x}^K} F(\bar{x}^K) \tag{22.5}$$

until the residuals are smaller than a predetermined error ε (i.e., $\left|f_i(\bar{x}^K)\right| \le \varepsilon$).

The Newton-Raphson solution is formulated by discarding one equation from the set described by equations (A1) through (A10). This is necessary because there are only nine independent equations out of the ten equations. Since for noisy data, these ten equations are inconsistent, a multiple solution set is obtained, with the solution depending on which equation is ignored.

Before the iterative approximation can be carried out, a good initial estimate if the unknown vector $\bar{x}$ is essential for convergence to a solution. In this study, the initialization of the unknown vector $\bar{x}$ is performed by using the method developed by Umans [15]. In his method, Equation (A8) (See Appendix A) is discarded and the remaining nine equations are solved for the nine parameters.

22.2.2.2 Estimation of q-axis Parameters

The q-axis transfer function of the SSFR3 equivalent circuit can be written as:

$$L_q(s) = K_q \frac{(1+T_1^{'}s)(1+T_2^{'}s)(1+T_3^{'}s)}{(1+T_4^{'}s)(1+T_5^{'}s)(1+T_6^{'}s)} \tag{22.6}$$

Using an assumed value of armature resistance, R_a, the $L_q(s)$ is calculated from the operational impedance, $Z_q(s) = -V_q(s) / I_q(s)$. The q-axis parameters can be determined from a consistent set of linear equations (see reference [15]) which relate the $L_q(s)$ transfer function's time constants to the equivalent circuit parameters.

22.2.3 STUDY PROCESS

For the purpose of this study, synthetic frequency response data were created using the Monticello generating unit SSFR3 model parameters derived by Dandeno [11]. The frequency response data so developed were then corrupted with a uniformly distributed noise of zero mean and varying degrees of signal to noise ratios. Following relationship were used in creating the noise-corrupted data:

$$\tilde{Z}_d(s) = Z_d(s) + \eta_1 \tag{22.7}$$

$$\tilde{Z}_q(s) = Z_q(s) + \eta_2 \tag{22.8}$$

$$s\tilde{G}(s) = sG(s) + \eta_3 \tag{22.9}$$

where $\tilde{Z}_d(s)$, $\tilde{Z}_q(s)$, and $s\tilde{G}(s)$ represent the noise-corrupted data, and η_1, η_2, and η_3 represent noise.

The noise-corrupted $\tilde{L}_d(s)$ and $\tilde{L}_q(s)$ data were then developed using the following relationships:

$$\tilde{L}_d(s) = \frac{\tilde{Z}_d(s) - R_a}{s} \tag{22.10}$$

$$\tilde{L}_q(s) = \frac{\tilde{Z}_q(s) - R_a}{s} \tag{22.11}$$

where R_a is the armature resistance originally used in creating the synthetic data.

Following this, the required d-q axes transfer functions were computed based on the nonlinear least square curve-fitting techniques developed by Marquardt [20]. Both magnitude and phase angle data were used in estimating the time constants. Monticello generator parameters, corresponding to the SSFR3 model structures, were then recalculated using the Newton-Raphson method discussed earlier. The same model structure was retained so that any discrepancy observed in the recalculated values of the machines parameters, could be specifically ascribed to the noise introduced in the synthetic data.

22.2.4 ANALYSIS OF RESULTS

For the purpose of evaluating the effect of noise on estimated parameters of the Monticello machine used as the study machine, various uniformly distributed noise sequence were used with zero mean and with signal to noise ratios (S/N) varying from 3100:1 to 250:1, where $S/N = (\Sigma(signal)^2/(noise)^2)^{1/2}$.

To assess the appropriate level of S/N ratio that should be considered in the study, an effort was made to roughly estimate the level of S/N ratio normally achievable in a SSFR field test. For this purpose, noise-corrupted synthetic data of the Monticello generator with S/N ratios ranging from 3100:1 to 250:1 were plotted and compared with the corresponding data acquired during the August 1984 test on Rockport Unit #1. This is a 1300 MW cross-compounded unit owned and operated by the American Electric Power Company.

Figure 22.2 shows the $L_d(s)$ magnitude and phase plots of the Rockport field test data and the noise-corrupted synthetic data of the Monticello generator with S/N ratio of 3100:1. The two sets of plots are similar, showing similar noise effects. Plots corresponding to S/N ratio of 250:1 were found to be too noisy, but because of space constrains are not included in this section. However, to evaluate the full impact of measurement noise, some results pertaining to such noisy data are also provided in this section.

22.2.4.1 D-axis Parameter Estimation

Table 22.2 shows estimated values of the d-axis transfer function time constants of the Monticello machine corresponding to various degrees of S/N ratios.

Results obtained indicate that because of the noise in the synthetic data, an error is introduced in the estimated values of the transfer function time constants. Moreover, the magnitude of the error increases significantly as the S/N ratio deteriorates (i.e., noise level is higher) from 3100:1 to 250:1.

The transfer function time constants corresponding to S/N ratio of 3100:1 were then used to estimate the d-axis machine parameters. For this purpose, the nonlinear set of equations (A1-A10) was solved using the Newton-Raphson method. As indicated earlier, these are a redundant and inconsistent set of equations with the number of unknowns being one less than the number of equations. Therefore, to obtain the solution, one of the equations has to be discarded. However, the authors of this chapter feel that there are no obvious reasons for discarding any particular equation. Therefore, in this study, an effort was made to solve the sub-sets of equations obtained by discarding one equation at a time.

Results presented in Table 22.3 indicate that by using this approach, four solution sets are obtained even when the S/N ratio is as high as 3100:1. In this case, the same solution set was

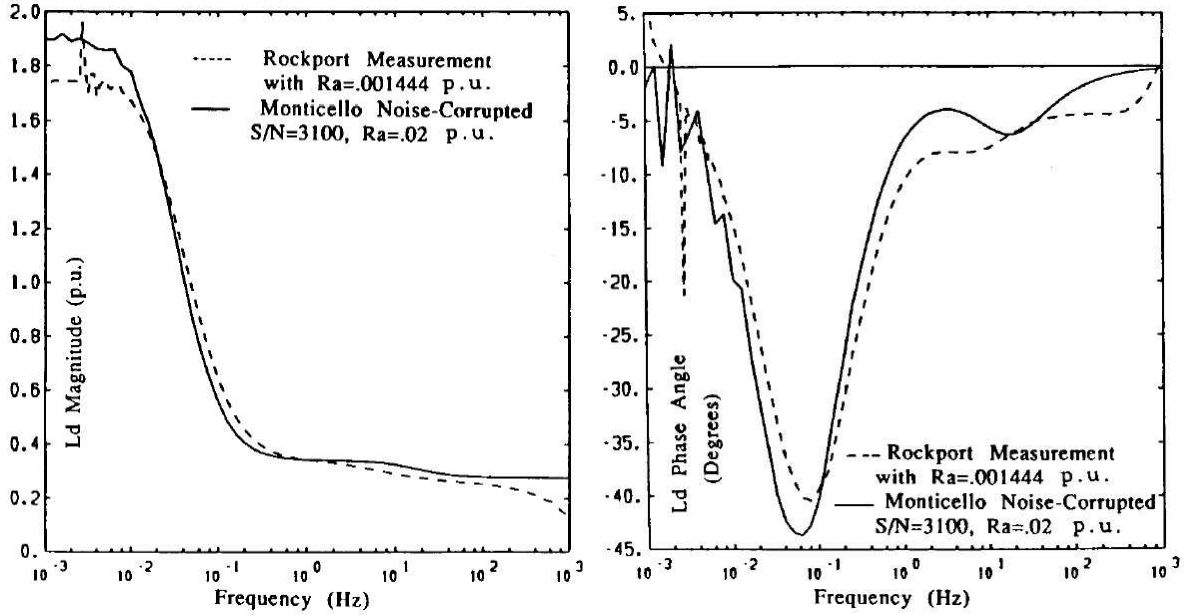

(a) $L_d(s)$ Magnitude (b) $L_d(s)$ Phase

Figure 22.2 $L_d(s)$ Magnitude and Phase Plots of Field Test and Synthetic Noise-Corrupted Data

Table 22.2 Estimated Values of d-axis Transfer Function Time Constants with R_a=0.02 p.u.

		Estimated Values Obtained with Ra = 0.02					
	Orgnl Values	S/N Ratio 3100:1		S/N Ratio 500:1		S/N Ratio 250:1	
TFT*	With Ra=0.02	Est.	% Error	Est.	% Error	Est.	% Error
K_d	1.9	1.9025	-0.13	2.0009	-5.31	2.2419	-18.0
T_1	1.184	1.1842	-0.01	1.1655	1.56	1.0645	10.09
T_2	0.00772	0.00772	0.05	0.00759	1.63	0.00779	-0.92
T_3	0.0026	0.00259	0.40	0.00245	5.72	0.00224	13.71
T_4	6.601	6.6121	-0.03	6.9155	-4.62	7.3178	-10.70
T_5	0.00951	0.00949	0.07	0.00917	3.42	0.00882	7.10
T_6	0.0026	0.0026	0.0	0.00248	4.47	0.00235	9.43
T_7	0.00453	0.00452	0.22	0.00421	6.56	0.00389	13.78
T_8	0.00041	0.00041	-0.01	0.0004	0.96	0.0004	1.88
G_d	5.5308	5.5387	-0.15	5.7649	-4.24	6.0636	-9.64

*TFT - Transfer Function Time Constants

obtained when Equation A.2-A.7 were discarded one at a time; no solution could be obtained when Equation A.1 was discarded.

A study of Table 22.3 indicates that some of the parameters in these solution sets differ by as much as 130%. In particular, the value of the generator field winding inductance (L_{fd}) in solution set 2 differs from its original value by as much as 42%. This means that for the same value of R_{fd}, the d-axis transient short circuit time constant will differ significantly from the original value.

Table 22.3 Estimated Values of d-axis Machine Parameters with S/N Ratio 3100:1 and R_a = 0.02 p.u.

Estimated Values of d-axis Machine Parameters
With S/N Ratio of 3100:1 and Ra = 0.02 p.u.

Machine Parameters in p.u.	Original Values	Estimated Values			
		Set 1* With EQD** of A2-A7	Set 2 With EQD of A8	Set 3 With EQD of A9	Set 4 With EQD of A10
L_{ad}	1.691	1.69352	1.69352	1.69352	1.69352
L_{f12d}	0.0093	0.00953	0.0103	0.00378	-0.00301
R_{1d}	0.067	0.06684	0.0671	0.07326	0.08013
L_{1d}	0.1144	0.11377	0.11422	0.13152	0.15096
L_{f2d}	0.1287	0.12826	0.12374	0.13323	0.14065
R_{2d}	0.0092	0.0091	0.01316	0.00899	0.00889
L_{2d}	0.0014	0.00139	0.00201	0.00054	0.00123
R_{fd}	0.00081	0.00081	0.00079	0.00081	0.00081
L_{fd}	0.0087	0.00864	0.01237	0.00942	0.00854
Res***	-	0.78	57.9	-0.15	0.17

*Solution obtained by discarding any one of the equations A2 through A7.
**EQD - Equation Number Discarded
***Res - This is residual of the discarded equation.

An effort was also mage to estimate the accuracy of each of these solution sets. For this purpose, frequency response data were created corresponding to each of the four solution sets. Data so obtained were compared with the noise-corrupted synthetic data of the Monticello machine. Accuracy was measured in terms of the Mean Error and the RMS Error which are defined as follows:

$$\text{Mean Error} = \frac{1}{n}\sum_{K=1}^{n} e_{(K)}$$

$$\text{RMS Error} = \sqrt{\frac{1}{n}\sum_{K=1}^{n} e_{(K)}^2}$$

where,

n = Number of data points

$e_{(K)}$ = (Value of the noise-corrupted synthetic data at the *Kth* frequency) – (Value of the created data corresponding to a particular solution set at the *Kth* frequency)

Results presented in Table 22.4 indicate that each of the solution sets is quite accurate; Mean error and RMS error of each solution set are quite small.

Therefore, it may be observed that by using frequency analytical techniques, multiple solution sets are obtained with each of the solution set being quite accurate. However,

Table 22.4 D-axis Mean and RMS Errors of Estimated Frequency Response with S/N Ratio of 3100:1 and R_a = 0.02 p.u.

Set No.	Mean Error		RMS Error	
	LD Magnitude	sG Magnitude	LD Magnitude	sG Magnitude
1	0.52E-05	0.35E-04	0.59E-02	0.22E-03
2	0.26E-04	0.14E-01	0.59E-02	0.16E-01
3	0.26E-04	-0.10E-02	0.59E-02	0.82E-02
4	0.26E-04	0.47E-02	0.59E-02	0.91E-02

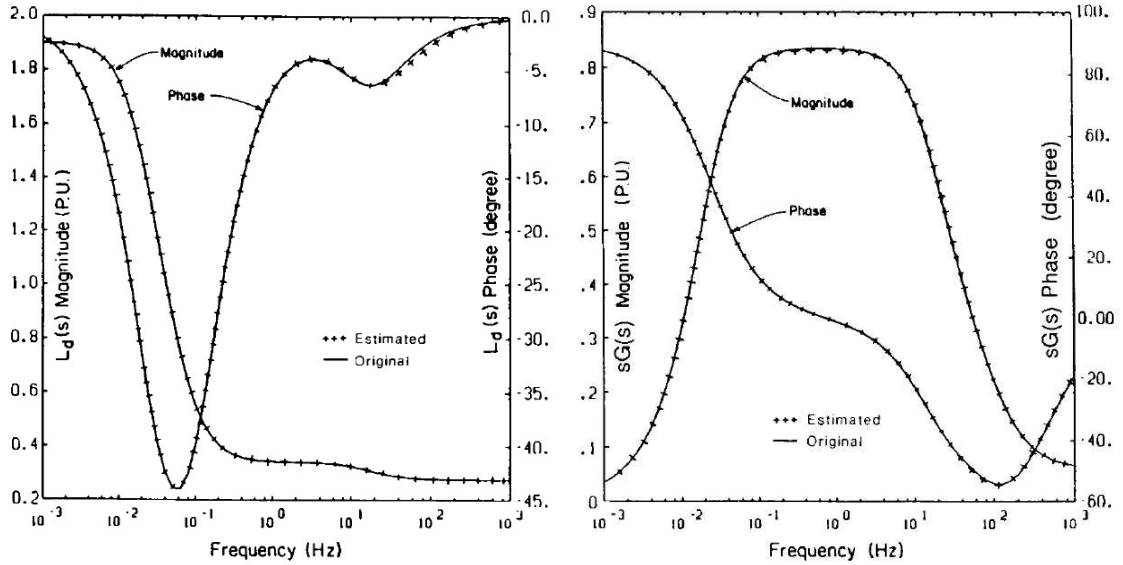

(a) $L_d(s)$ Variation (b) $sG(s)$ Variation

Figure 22.3 Monticello Synthetic Noise-Corrupted and Estimated Variation of $L_d(s)$ and $sG(s)$ with Frequency

estimated values of some of the machine parameters may differ significantly from the corresponding values in the other solution sets. In view of this, it may sometimes be difficult to choose a solution from the multiple solution sets.

Figure 22.3 shows the noise-corrupted synthetic data plots of $L_d(s)$ and $sG(s)$ generated from the original values of the Monticello machine parameters given in Table 3. These plots are superimposed the frequency response data generated from the estimated values of the machine parameters shown in the solution set 1 in Table 3. The two sets of plots overlap each other almost completely. This confirms a high degree level of accuracy can be shown to exist for the other solution sets.

For each of the transfer function time constant sets shown in Table 22.2, corresponding to d-axis machine parameters were estimated. The machine parameters obtained by discarding Equation number A.8 are presented in Table 22.5. It may be noted that Equation A.8 corresponds to the equation discarded by Umans in reference [16].

The purpose of obtaining these parameters by discarding only one particular equation is to specifically study the impact of noise in the test data while circumventing the multiple solution set issue.

Table 22.5 Estimated Values of D-Axis Machine Parameters with R_a = 0.02 p.u. and Discarding Equation A.8

Machine Parameters in p.u.	Original Values With Ra = 0.02	Estimated Values Obtained With Ra = 0.02 p.u.		
		S/N Ratio 3100:1	S/N Ratio 500:1	S/N Ratio 250:1
L_{ad}	1.691	1.69352	1.79189	2.03293
L_{f12d}	0.0093	0.01030	0.02429	0.06845
R_{1d}	0.067	0.06710	0.06624	0.07578
L_{1d}	0.1144	0.11422	0.10521	0.11107
L_{f2d}	0.1287	0.12374	0.07407	-0.00502
R_{2d}	0.0092	0.01316	0.03978	0.03237
L_{2d}	0.0014	0.00201	0.00603	0.00486
R_{fd}	0.00081	0.00079	0.00076	0.00081
L_{fd}	0.0087	0.01237	0.04327	0.06467
Res*	0.0	57.9	176	245

*Res - This is residual of the discarded equation.

A study of Table 22.5 indicates that as the S/N ratio deteriorates, estimated values of some of the machine parameters vary significantly. In particular, for the case of S/N ratio of 250:1, values of L_{ad}, L_{f2d} and L_{fd} become unrealistic. This is primarily because noise in the test data introduces error in the estimated values of the transfer function time constants. This error is then amplified during the process of estimating machine parameters from the sub-set of Equations A.1-A.10.

During this study, an effort was also made to assess sensitivity of the estimated values of the machine parameters, to the error in the value of armature resistance R_a used in deriving the operational inductance $L_d(s)$ from the operational impedance $Z_d(s)$ data.

The value of R_a is generally calculated from the low frequency asymptote of the $Z_d(s)$ or $Z_q(s)$ data (i.e., $R_a = Lim_{s->0} Z_d(s)$). However, experience shows that the data resolution is very poor in the low frequency range. Therefore, calculated value of R_a is bound to have certain degree of error. This will be true to some extent when R_a is measured directly with the help of a sensitive bridge circuit.

In view of the above fact, the machine parameters were estimated for two sets of values of R_a, i.e., 0.02 p.u. and 0.0201 p.u.. The corresponding results obtained are presented in Tables 22.5 and 22.6.

A study of Table 22.6 shows that when the value of R_a is 0.0201 p.u. instead of 0.02 p.u., the machine parameters estimated become unrealistic even when then S/N ratio is as high as 3100:1. L_{ad}, which can be measured quite accurately with the help of a number of well-established testing procedures, is approximately 60% higher than the original value used for generating the synthetic data. The value of L_{fd} is negative, which is totally unrealistic. Similarly, a negative value of R_{2d} cannot be justified.

Therefore, these results clearly show that estimated values of the machine parameters are very sensitive to the value of R_a. Even a 0.5% error in R_a could result in unrealistic estimation of the machine parameters.

Table 22.6 Estimated Values of D-Axis Machine Parameters with R_a = 0.0201 p.u. and Discarding Equation A.8

Machine Parameters in p.u.	Original Values With Ra = 0.02	Estimated Values Obtained With Ra = 0.0201 p.u.		
		S/N Ratio 3100:1	S/N Ratio 500:1	S/N Ratio 250:1
L_{ad}	1.691	2.69676	2.73873	2.85214
L_{f12d}	0.0093	0.22544	0.23764	0.24937
R_{1d}	0.067	0.12913	0.14289	0.16692
L_{1d}	0.1144	0.1778	0.19490	0.21758
L_{f2d}	0.1287	-0.08238	-0.08943	-0.09757
R_{2d}	0.0092	-0.01695	-0.01894	-0.02134
L_{2d}	0.0014	-0.0025	-0.00281	-0.00315
R_{fd}	0.00081	0.0009	0.00091	0.00093
L_{fd}	0.0087	-0.05903	-0.06577	-0.07234
Res*	0.0	571	569	582

*Res - This is residual of the discarded equation.

It may be noted that noise, inherent in the test data, is a random process and cannot be removed. In practice, one can only remove unwanted signals, which are not part of the system to be modeled, by using filters (hardware or software filters). Therefore, to minimize the effect of noise, the analytical technique used should be robust and should not be affected by noise.

A study of the q-axis parameters estimation gives similar results as above.

22.2.5 CONCLUSIONS

Based on the results of this study, it is concluded that:

1) Noise, which is inherently present in the field test data, has significant impact on the synchronous machine parameters estimated from the SSFR test data using curve-fitting techniques.
2) Multiple solution sets for the machine parameters are obtained depending upon the equation ignored from the set of relevant equations. In some cases the solution may not even converge.
3) Estimated values of the machine parameters are very sensitive to the vales of armature resistance used in the data analysis. Even a 0.5% error in the value of armature resistance could result in unrealistic estimation of the machine parameters.
4) A technique should be developed which provides a unique physically realizable machine model even when the test data are noise-corrupted. This problem is studied in the next section.

22.3 MAXIMUM LIKELIHOOD ESTIMATION OF SOLID-ROTOR SYNCHRONOUS MACHINE PARAMETERS

22.3.1 INTRODUCTION

In the previous section, it was shown that multiple parameter sets will be obtained when the transfer functions of a solid-rotor synchronous machine are estimated from noise-corrupted, frequency-domain data and then, the machine parameters are computed from the estimated machine transfer function's time constants. Moreover, the estimated machine parameters are very sensitive to the value of the armature resistance used in the study.

In this section, a time-domain identification technique is used to estimate machine parameters. The objective is to show that the multiple solution set problem encountered in the frequency response technique can be eliminated if the time-domain estimation data are generated from the d-q axis transfer functions estimated for the SSFR test data. The maximum likelihood (ML) estimation technique is then used to estimate the machine parameters.

The ML identification method has been applied to the parameter estimation of many engineering problems [25-30]. It has been established that the ML algorithm has the advantage of computing consistent parameter estimates from noise-corrupted data. This means that the estimate will converge to the true parameter values as the number of observations goes to infinity [29-30]. This is not the case for the least-square estimators which are commonly used in power system applications.

22.3.2 STANDSTILL SYNCHRONOUS MACHINE MODEL FOR TIME-DOMAIN PARAMETER ESTIMATION

22.3.2.1 D-Axis Model

Assuming that the d-axis rotor body can be represented by two damper windings (i.e., SSFR3), the standstill discrete d-axis model of a round rotor machine is given by [19]:

$$X(k+1) = A_d(\theta_d)X(k) + B_d(\theta_d)U(k) + w(k) \tag{22.12}$$

$$Y(k+1) = C_d X(k+1) + v(k+1) \tag{22.13}$$

where

$$C_d = \begin{bmatrix} 1 & 0 & 0 & 0 \\ 0 & 0 & 0 & 1 \end{bmatrix}$$

$$X = \begin{bmatrix} i_d & i_{1d} & i_{2d} & i_{fd} \end{bmatrix}^T$$

$$Y = \begin{bmatrix} i_d & i_{fd} \end{bmatrix}, \quad U = \begin{bmatrix} v_d \end{bmatrix}$$

$$\theta_d = \begin{bmatrix} L_{ad}, L_{f12d}, R_{1d}, L_{1d}, L_{f2d}, R_{2d}, L_{2d}, R_{fd}, L_{fd} \end{bmatrix}$$

In addition, $w(\cdot)$ and $v(\cdot)$ denote the process noise and measurement noise respectively. It is assumed that

$$E[w] = 0, \quad Q = E[ww^T] \tag{22.14}$$

$$E[v] = 0, \quad R_0 = E[vv^T] \tag{22.15}$$

$$E[X[0]] = [0], \quad P_0 = E[XX^T] \tag{22.16}$$

22.3.2.2 Q-Axis Model

Assuming that the q-axis rotor body can be represented by three damper windings, the standstill discrete q-axis model is given by:

$$X(k+1) = A_q(\theta_q)X(k) + B_q(\theta_q)U(k) + w(k) \tag{22.17}$$

$$Y(k+1) = C_q X(k+1) + v(k+1) \tag{22.18}$$

where

$$C_d = [1 \quad 0 \quad 0 \quad 0]$$

$$X = [i_q \quad i_{1q} \quad i_{2q} \quad i_{3q}]^T$$

$$Y = [i_q], \; U = [v_q]$$

$$\theta_q = [L_{aq}, R_{1q}, L_{1q}, R_{2q}, L_{2q}, R_{3q}, L_{3q}]$$

The initial value of the state and statistics of measurement noise are described by Equation 22.14 through Equation 22.16. The computations of $A_d(\theta_d), B_d(\theta_d), A_q(\theta_q), B_q(\theta_q)$ from the continuous time-domain representation are described in [19], and the explicit parameterization in terms of θ_d and θ_q are shown in Appendix B.

In this study, the effect of noise on parameter estimation is studied by using the simulated noisy data of a known model structure for parameter identification. The identification problem is to estimate the parameter vector θ_d and θ_q from a record of the time-domain sequence of i_d, i_{fd}, i_q, v_d and v_q.

22.3.3 EFFECT OF NOISE ON THE PROCESS AND THE MEASUREMENT

Figure 4 shows the block diagram of the effect of noise on the process and the measurements. The model, which mathematically describes the process, is subjected to the deterministic input at each time instant *k*. Nature also subjects the process to a random input sequence $w(\cdot)$. The sequence $w(\cdot)$ is designated as the process noise sequence. It is assumed to be Gaussian with zero mean and covariance matrix $Q(\cdot)$. The covariance matrix Q gives a measure of the intensity of the process noise on the model. A high value of the covariance matrix Q corresponds to a noisy process. The reason for introducing the measurement noise sequence $v(\cdot)$ is that in physical problems, the measurements are inherently subjected to errors.

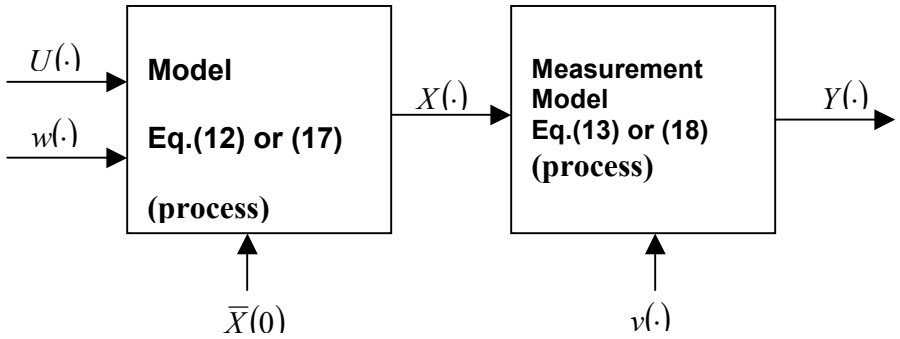

Figure 22.4 Block Diagram Representation of Measurement and Process Noise

The signal conditioning equipment and sensors introduce measurement noise, which is random. The measurement errors $v(\cdot)$ are assumed to be independent and Gaussian with zero mean value and a known covariance matrix R_0. It is further assumed that the sequence $w(\cdot)$, $v(\cdot)$, and $X(0)$ are independent.

Let us denote the variance of $v_1(\cdot)$ and $v_2(\cdot)$ by $\sigma_{v_1}^2$ and $\sigma_{v_2}^2$. Also let $v_1(\cdot)$ and $v_2(\cdot)$ represent the measurement noise of i_d and i_{fd}. The assumption that $v_1(\cdot)$ and $v_2(\cdot)$ are independent ensures that measurement of i_d will not introduce additional uncertainty (i.e., measurement noise) in the measurement of i_{fd}. This assumption is not completely true. For example, the use of shunt resistances for current measurements will introduce its own uncertainty in the process variables to be measured. In this book, however, it is assumed that measurement errors are independent; therefore the covariance $R(\cdot)$ is a diagonal matrix, and the diagonal elements represent the variance of the measurement errors. Note that the standard deviations of measurement errors represent the percent errors associated with the sensors. The accuracy of the sensors may be known from the "manufacturer data" or from carefully controlled experiments on the sensors themselves.

The initial covariance R_0 is constructed from the knowledge of sensor errors, and it represents a measure of the prior confidence in the sensors to produce accurate measurements. Strictly speaking, two experiments performed on the same process will not result in identical measurements. Therefore, the covariance of the estimation error is calculated as part of Kalman filter [26-30] for estimating the machine states and then the parameters. The covariance of the estimation error is defined as

$$\begin{aligned} R(k) &= COV(e(k), e(k)) \\ e(k) &= Y(k) - \hat{Y}(k) \end{aligned} \tag{22.19}$$

22.3.4 MAXIMUM LIKELIHOOD PARAMETER ESTIMATION

Consider the system described by the linear difference Equations 22.12 and 22.13 or 22.17 and 22.18. To apply the maximum likelihood (ML) method, the first step is to specify the likelihood function [26-30]. The likelihood function $L(\theta)$, where θ represents θ_d or θ_q, is defined as

$$L(\theta) = \prod_{k=1}^{N} \left[\frac{1}{\sqrt{(2\pi)^m \det(R(k))}} \exp\left(-\frac{1}{2} e(k)^T R(k)^{-1} e(k) \right) \right] \tag{22.20}$$

where $e(\cdot)$, $R(\cdot)$, N and m denotes the estimation error, the covariance of the estimation error (see Equation 22.19), the number of data points, and the dimension of Y, respectively.

Maximizing $L(\theta)$ is equivalent to minimizing its negative log function, which is defined as:

$$V(\theta) = -\log L(\theta)$$
$$V(\theta) = \frac{1}{2}\sum_{k=1}^{N}\left[e(k)^T R(k)^{-1} e(k)\right] + \frac{1}{2}\sum_{k=1}^{N}\log\det(R(k)) + \frac{1}{2}mN\log(2\pi) \tag{22.21}$$

The vector θ (i.e., θ_d or θ_q) can be computed iteratively using Newton's approach [27,31]:

$$H\Delta\theta + G = 0$$
$$\theta_{new} = \theta_{old} + \Delta\theta \tag{22.22}$$

where H and G are the Hessian matrix and the gradient vector of $V(\theta)$. They are defined by:

$$H = \frac{\partial^2 V(\theta)}{\partial\theta^2} \quad G = \frac{\partial V(\theta)}{\partial\theta} \tag{22.23}$$

The H and G matrices are calculated using the numerical finite difference method as described in [24,30].

To start iterative approximation of θ, the covariance of estimation error $R(k)$ (see Eq. (19)) is obtained using the Kalman filter theory [25-29]. The steps are as follows:

1. Initial conditions: The initial value of the state is set equal to zero. The initial covariance state matrix P_0 is assumed to be a diagonal matrix with large positive numbers. Furthermore, assume an initial set of parameter vector θ.

2. Using the initial values of the parameters vector θ, compute the matrices A, B, and C for d or q-axis.

3. Compute estimate $\hat{Y}(k \mid k-1)$ from $\hat{X}(k \mid k-1)$:

$$\hat{Y}(k \mid k-1) = C\hat{X}(k \mid k-1) \tag{22.24}$$

4. Compute the estimation error of $Y(k)$:

$$e(k) = Y(k) - \hat{Y}(k \mid k-1) \tag{22.25}$$

5. Compute the estimation error covariance matrix $R(k)$:

$$R(k) = R_0 + C \cdot P(k \mid k-1) \cdot C^T \tag{22.26}$$

6. Compute the Kalman gain matrix:

$$K(k) = P(k \mid k-1) \cdot C^T \cdot R(k)^{-1} \tag{22.27}$$

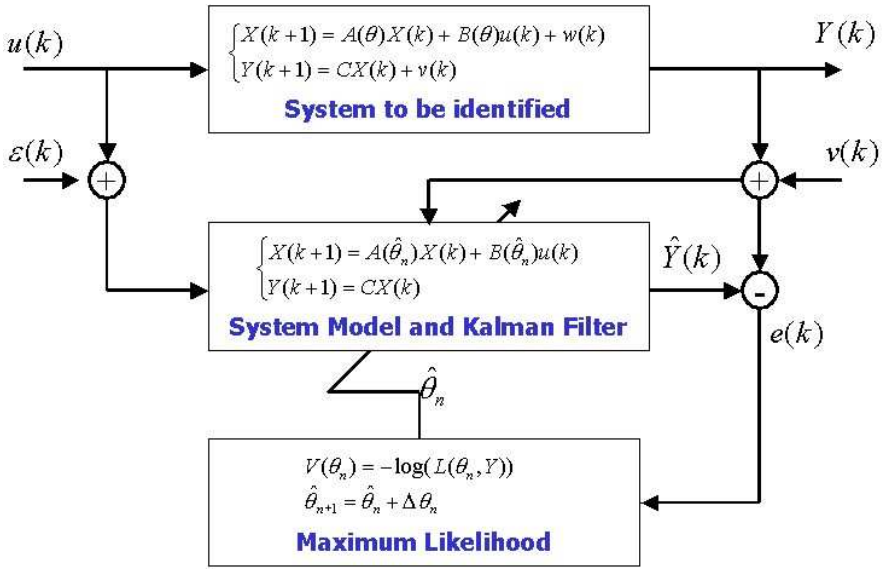

Figure 22.5 Block diagram of Maximum Likelihood Estimation

7. Compute the state estimation covariance matrix at instant k and k+1:

$$P(k \mid k) = P(k \mid k-1) - K(k) \cdot C \cdot P(k \mid k-1)$$
$$P(k+1 \mid k) = A(\theta) \cdot P(k \mid k) \cdot A^T(\theta) + Q \qquad (22.28)$$

8. Compute the state at instant k and k+1:

$$\hat{X}(k \mid k) = \hat{X}(k \mid k-1) + K(k) \cdot e(k)$$
$$\hat{X}(k+1 \mid k) = A(\theta) \cdot \hat{X}(k \mid k) + B(\theta) \cdot U(k) \qquad (22.29)$$

9. Solve Eq. (22) for $\Delta\theta$ and compute the new θ such that

$$\theta_{\min} \le \theta_{new} \le \theta_{\max} \qquad (22.30)$$

10. Repeat steps 2 through 9 until $V(\theta)$ is minimized.

The above mechanism for maximum likelihood estimation is illustrated in Figure 5. A model of the system is excited with the same input as the real system. The error between the estimated output and the measured output is used to adjust the model parameters to minimize the error (maximize the likelihood). This process is repeated till the cost function $V(\theta)$ is minimized.

22.3.5 ESTIMATION PROCEDURE USING SSFR TEST DATA

The machine parameters estimated from the frequency-domain data are very sensitive to the value of the armature resistance used in deriving the operational inductance L_d and L_q data

[22]. However, the values of L_{ad} and L_{aq} provided by manufactures are quite accurate. In our estimation of rotor body circuit parameters, the manufacturer's specified values of L_{ad} and L_{aq} will be utilized to decide the appropriate value for armature resistance. The θ_{min} and θ_{max} (e.g., $L_{ad,min}$ and $L_{ad,max}$) are selected within $\pm 15\%$ of the values supplied by the manufacturers. The rotor body circuit parameters are constrained to be greater than zero. The steps are as follows:

1. Estimate the value of R_a :

$$R_a = \lim_{\omega \to 0} Z_d(j\omega)$$

2. Compute the operational inductance L_d and L_q data using the measured frequency response data or Z_d and Z_q.
3. Fit very high-order transfer function to $L_d(s)$ and $L_q(s)$ data of step 2 and $sG(s)$ transfer function [22].
4. Compute the step-response of the transfer function of step 3.
5. Use the *ML* identification technique to estimate the machine parameters as a constraint minimization problem.

As indicated in the previous section, the transfer function's time constants are very sensitive to the value of R_a. If the initial value of R_a is not accurately estimated, then this may not give a minimum value of $V(\theta)$. Therefore, it is suggested that the constraint *ML* identification process be repeated for another value of R_a until $V(\theta)$ is minimized.

This problem of iterating with different values of R_a occurs only when the time-domain data are generated from the SSFR test data. If the time-domain data are directly measured, all parameters can be estimated without going through the above iterative procedure.

It may be noted that accurate results will be obtained by this approach, because in step 3 high order transfer functions can be fitted to the $L_d(s)$, $L_q(s)$, and $sG(s)$ data. In the classical frequency response technique, only the third- or second-order transfer functions are used. Therefore the estimated transfer functions will not accurately represent the SSFR data in the subtransient region [11]. Furthermore, as indicated in the previous section, multiple parameter sets will be obtained when the machine parameters are estimated using the classical SSFR technique. Note that the use of higher order transfer functions, in the classical SSFR technique, will result in a larger set of nonlinear and inconsistent equations (see Appendix A) which cannot be accurately solved for the machine parameters. However, the proposed approach can be used to obtain an accurate and unique estimation of machine parameters.

22.3.6 RESULTS

The machine parameters are estimated from the time-domain data, which are computed by using the estimated transfer functions. The transfer functions are estimated from the noise-corrupted SSFR data as described in previous section. The signal-to-noise ratio of 3100:1 (where $S/N = [\Sigma(signal)^2/(noise)^2]^{1/2}$) is used in this study. The noise sequence used is a normally distributed random variable with zero mean.

To obtain a record of the time-domain data, the step response of the estimated d-q axis transfer functions [1] is computed. The input step voltage is defined as

$$V_d(t) = \begin{cases} 1 & t \le 0.025s \\ 0 & t > 0.025s \end{cases}$$
$$V_q(t) = \begin{cases} 1 & t \le 0.06s \\ 0 & t > 0.06s \end{cases} \tag{22.31}$$

The input signals to be applied to the transfer functions can be chosen without any constraints. The step voltage signals are used because of their rich frequency contents. This input signal excited all the estimated transfer function modes. The time-domain data of $i_d(\cdot)$, $i_{fd}(\cdot)$ and $i_q(\cdot)$ are computed using the input step defined by Eq. (31). The variance of the process noise is assumed to be negligible, and its signal-to-noise ratio is very high. The signal-to-noise ratio of measurement noise is 3100:1. This measurement noise was introduced in the SSFR data.

The ML estimation is used to estimate the machine parameters. The results are given in Table 22.7 for d-axis, and in Table 22.8 for q-axis. The parameters L_{ad}, L_{aq}, and R_{fd} were initialized at 15% below their original values. Since the ranges of these variables are known, the initial values of these parameters are quite reasonable. However, since a priori knowledge of the rotor body circuits' parameters is much less precise, they are initialized arbitrarily.

Table 22.7 Maximum Likelihood Identification of D-Axis Parameters

SSFR3 Parameter p.u.	Initial Values	Estimated Values	Original Values	Percent Errors
L_{ad}	1.4400E-0	1.6933E-0	1.691E-0	0.1
L_{f12d}	1.0000E-1	9.7909E-3	9.3E-3	5.0
R_{1d}	1.0000E-1	6.6717E-2	6.7E-2	0.5
L_{1d}	1.0000E-1	1.1355E-1	1.144E-1	0.8
L_{f2d}	1.0000E-1	1.2801E-1	1.287E-1	0.5
R_{2d}	1.0000E-1	9.0980E-3	9.15E-3	0.5
L_{2d}	1.0000E-1	1.3919E-3	1.400E-3	0.5
Rfd	7.0000E-4	8.1093E-4	8.11E-4	0.0
L_{fd}	1.0000E-2	8.6397E-3	8.70E-3	0.7

Table 22.8 Maximum Likelihood Identification of Q-Axis Parameters

SSFR3 Parameters p.u.	Initial Values	Estimated Values	Original Values	Percent Errors
L_{aq}	1.440E-0	1.6328E-0	1.627E-0	0.4
R_{1q}	1.000E-1	1.0619E-2	1.06E-2	0.0
L_{1q}	1.000E-1	1.9245E-0	1.918E-0	0.4
R_{2q}	1.000E-1	1.3004E-1	1.293E-1	0.5
L_{2q}	1.000E-1	1.2584E-1	1.247E-1	0.9
R_{3q}	1.000E-1	2.1050E-2	2.10E-2	0.2
L_{3q}	1.000E-1	3.8318E-1	3.816E-1	0.4

The estimated parameters can be evaluated by comparing the mean and RMS errors of the $i_d(t)$, $i_{fd}(t)$, and $i_q(t)$ for both methods; namely, the SSFR method as stated in previous section and by the ML method.

It is established [29,30] that the ML method gives unique solution even when the data are noise-corrupted. The unique estimated values of the d-q axis parameters obtained in this study are given in Tables 22.7 and 22.8.

Figures 22.6-22.8 show that the time domain simulated responses of $i_d(t)$, $i_{fd}(t)$, and $i_q(t)$ respectively as step voltage are used as input in the d- and q-axis models of the Monticello machine. In each figure, three sets of responses are plotted. One of the responses corresponds to the original set of parameters of the Monticello machine, estimated in [11]. The remaining two sets of responses correspond to the parameters estimated by the ML and SSFR methods.

Figure 22.6 Monticello GS, Original and Estimated $i_d(t)$.

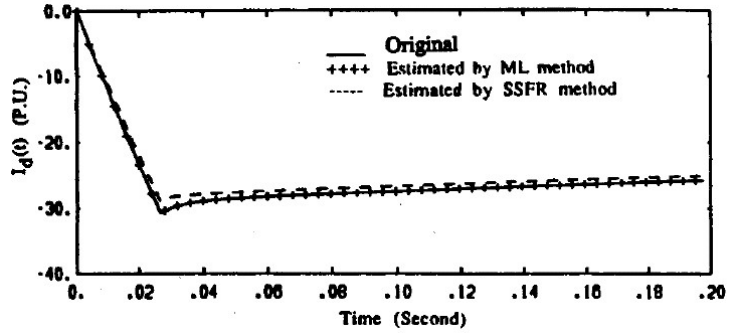

Figure 22.7 Monticello GS, Original and Estimated $i_{fd}(t)$.

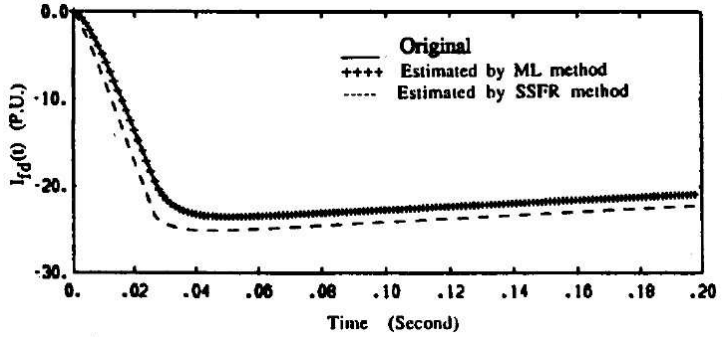

Figure 22.8 Monticello GS, Original and Estimated $i_q(t)$.

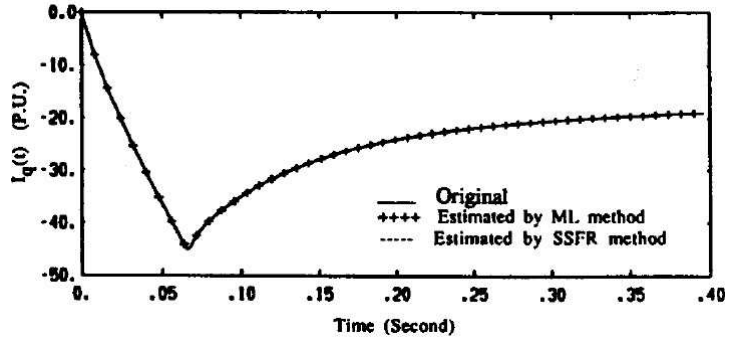

Table 22.9 Mean and RMS Error Comparisons of D-Axis and Q-Axis Time-Domain Response

	Method	Parameter Set	Mean Errors $i_d(t)$	Mean Errors $i_{fd}(t)$	RMS Errors $i_d(t)$	RMS Errors $i_{fd}(t)$
D-axis	SSFR [1]	1	9.5E-4	6.6E-3	1.0E-3	7.0E-3
		2	1.5E-1	1.0E-0	1.6E-1	1.0E-0
		3	6.9E-3	6.0E-3	2.1E-3	1.8E-2
		4	1.1E-2	6.9E-2	2.3E-2	1.5E-1
	ML	1	8.0E-4	5.5E-7	4.1E-5	6.1E-6

	Method		Mean Error $i_q(t)$	RMS Errors $i_q(t)$
Q-axis	SSFR		4.8E-8	1.2E-7
	ML		4.8E-8	1.2E-7

A study of these figures and Table 22.9 shows that for the same set of synthetic SSFR data, the d-axis results obtained by using the ML method are more accurate; and the q-axis results are the same for both methods. However, it can be shown that if an actual measured set of SSFR test data is used, the q-axis results of the ML method will also be more accurate. This is because, with the ML method, transfer functions higher than third order will represent the measured data more closely. Using higher order transfer functions will provide more accurate results both in the d- and q-axis parameters. It should be noted that the synthetic SSFR data used in this study were created from the SSFR3 model provided in [11]. Therefore, the transfer functions estimated to represent the noise-corrupted synthetic data could only be of third order.

The proposed approach can also be applied directly to measured standstill time test data. The standstill test data can be obtained by closing a suitable DC source across the stator windings while the field winding is short-circuited [6] so as to introduce a step change in voltage. The rotor position and stator connections are the same as SSFR testing procedures described in [6,11]. The ML technique can be used to estimate the armature, field and rotor body parameters directly from the measured standstill test data.

22.4 MODELING AND PARAMETER IDENTIFICATION OF INDUCTION MACHINES

Induction motors are used in automotive applications, either as stand-alone propulsion systems (electric vehicles) or in combination with an internal combustion engine (hybrid electric vehicles). Accurate knowledge of the induction motor model and its parameters is critical when field orientation techniques are used. The induction motor parameters vary with the operating conditions, as is the case with all electric motors. The inductances tend to

saturate at high flux levels and the resistances tend to increase as an effect of heating and skin effect. Temperature can have a large span of values, load can vary anywhere from no-load to full load and flux levels can change as commanded by an efficiency optimization algorithm. It could then be expected that the model parameters also vary considerably.

22.4.1 MODEL IDENTIFICATION

Although there are many models to describe induction motors, some are highly complex and not suitable to be used in control. The authors will only concentrate on the models that can be used in induction motor control. Also, since modern induction motor control is field oriented, d-q models will be analyzed. An excellent presentation on available model types can be found in [34]. The classical induction motor model (used in most control schemes) has identical d and q axis circuits, as shown in the Figure 22.9. Since the classical model is a fourth order system with 6 elements of storage (inductances) the model can be reduced to a simpler model without any loss of information [34].

The notations represent:

v_{ds}, v_{qs} : stator voltages in stationary reference frame

i_{ds}, i_{qs} : currents in stationary reference frame

$\lambda_{dr}, \lambda_{qr}$: rotor fluxes in stationary reference frame

L_l , L_m: magnetizing and leakage inductance (r for rotor s for stator)

R_s, R_r : stator, rotor resistance

ω_r : synchronous and mechanical frequency (*rad/s*).

The transformation combines the leakage inductances in a single inductance. This schematic is preferred for control applications and is called the Γ model (the classical model is denoted as the T model). Depending on whether a stator flux or rotor flux controller is sought the leakage inductance can be placed in the stator or in the rotor. The transformation is meant to have $L_{m'}$ be equal either to L_s or L_m of the classical model. Figure 22.10 shows the reduced model for rotor flux oriented (RFO) control.

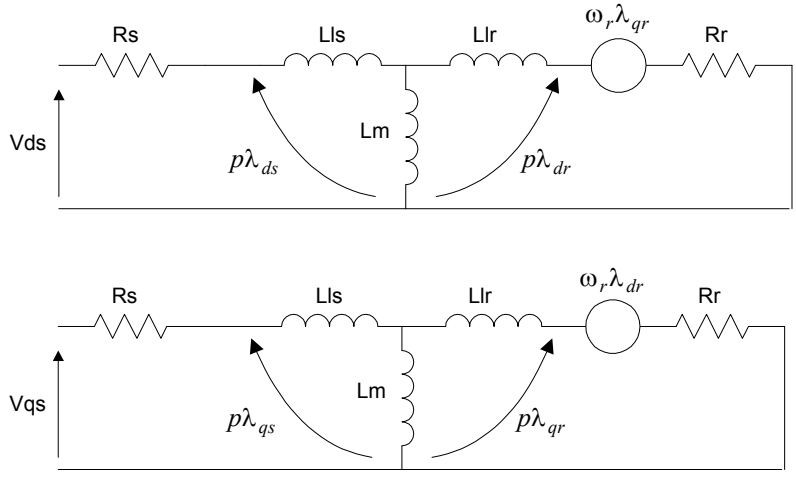

Figure 22.9 Equivalent circuits in d-q stationary

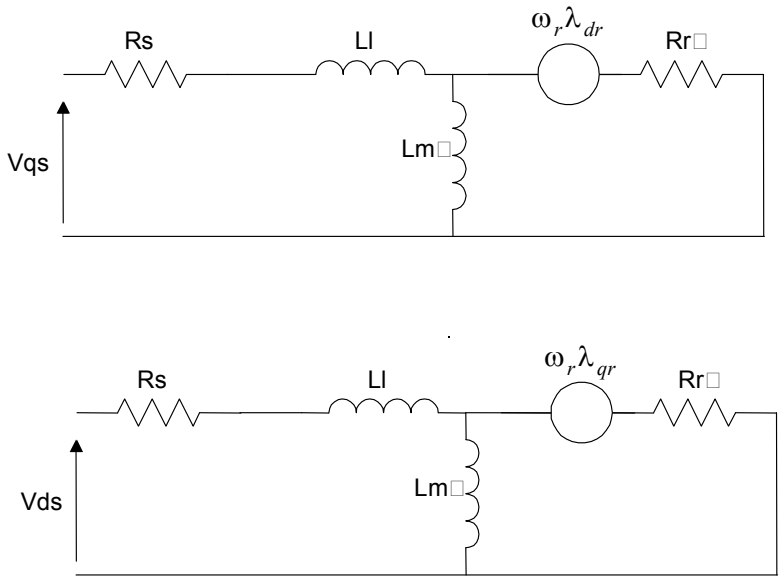

Figure 22.10 Reduced equivalent circuits in d-q stationary for RFO control

Although more complicated models, used in performance analysis, transient stability and short circuit studies exist, their complexity (expressed in the number of differential equations used in the model) makes them unattractive for control purposes. The known variations of the classical model are derived by allowing parameter variations and by representing core losses. Although all parameters are known to vary with the operating conditions, the effect of the variation of the leakage inductances is usually neglected. The magnetizing inductance is shown to vary as a function of the magnetizing current, rotor flux, or input voltage. The stator and rotor resistances are mainly affected by the rotor temperature and skin effect. In steady state models, core losses are typically represented as a resistance in parallel with the magnetizing inductance. However, by doing so the order of the model increases by two and adversely affects the control task. In literature, there are two trends to avoid this problem. One consists in adding the core loss resistance in parallel with the rotor resistance. The other, [34] adds an R-L branch in both d and q axis and supplies it with the voltage created by the rotor flux of the corresponding axis. Then the differential terms associated with this branch are neglected to maintain the order of the system. A third method consists in adding the core loss resistance in series with the magnetizing inductance.

Figure 22.11 shows the induction motor model used in this work in stationary reference frame. The core loss branch is added to account for both stator and rotor core losses. Since the core loss resistance is much larger than the rotor resistance, it will be neglected in this part of modeling. The following basic equations of induction machine can be derived:

$$\frac{d\omega_r}{dt} = \mu\left(\lambda_{dr} i_{qs} - \lambda_{qr} i_{ds}\right) - \frac{B}{J}\omega_r - \frac{T_L}{J} \tag{22.32}$$

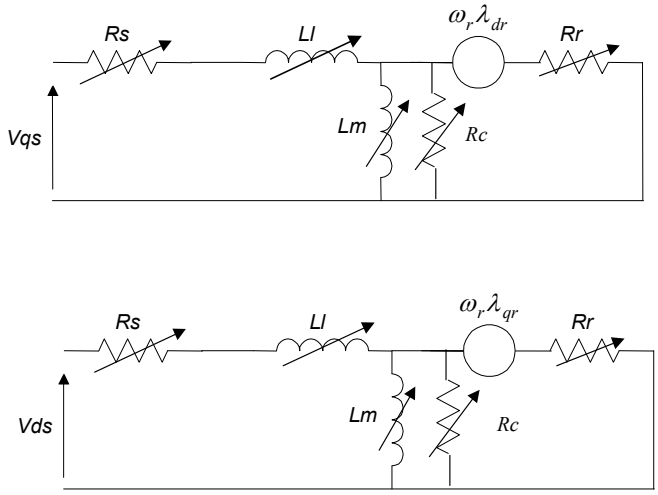

Figure 22.11 Induction motor models in stationary reference frame

$$\frac{d\lambda_{qr}}{dt} = n_p\omega_r\lambda_{dr} - \eta\lambda_{qr} + \eta L_m i_{qr} \tag{22.33}$$

$$\frac{d\lambda_{dr}}{dt} = -n_p\omega_r\lambda_{qr} - \eta\lambda_{dr} + \eta L_m i_{dr} \tag{22.34}$$

$$\frac{di_{qs}}{dt} = -\beta n_p\omega_r\lambda_{dr} + \eta\beta\lambda_{qr} - \gamma i_{qs} + \frac{1}{\sigma L_s}v_{qs} \tag{22.35}$$

$$\frac{di_{ds}}{dt} = \beta n_p\omega_r\lambda_{qr} + \eta\beta\lambda_{dr} - \gamma i_{ds} + \frac{1}{\sigma L_s}v_{ds} \tag{22.36}$$

where:

$\eta \equiv \dfrac{1}{T_R} = \dfrac{R_r}{L_m}$: inverse of the rotor time constant

$\sigma \equiv 1 - \dfrac{L_m}{L_s}$: leakage coefficient

$\beta \equiv \dfrac{1}{L_l}$: inverse of leakage inductance

$\gamma \equiv \dfrac{R_s + R_r}{L_l}$: inverse of the stator time constant

$L_s = L_l + L_m$: stator inductance

n_p : number of poles pairs

The electromagnetic torque expressed in terms of the state variables is:

$$T_e = \mu J\left(\lambda_{dr} i_{qs} - \lambda_{qr} i_{ds} \right) \tag{22.37}$$

where:

$\mu \equiv \frac{n_p}{J}$: constant

J: inertia of the rotor

T_e: electromagnetic torque ($N \cdot m$)

In synchronously rotating reference frame, the motor equations can be expressed as:

$$\frac{d\omega_r}{dt} = \mu \cdot \lambda_r \cdot i_{qs}^e - \frac{B}{J}\omega_r - \frac{T_L}{J} \tag{22.38}$$

$$\frac{d\lambda_r^e}{dt} = -\eta \cdot \lambda_r + \eta \cdot L_m \cdot i_{ds}^e \tag{22.39}$$

$$\frac{di_{qs}^e}{dt} = -\gamma i_{qs}^e - \beta n_p \omega_r \lambda_r - n_p \omega_r i_{ds}^e - \eta L_m \frac{i_{qs}^e i_{ds}^e}{\lambda_r} + \frac{1}{\sigma L_s} v_{qs}^e \tag{22.40}$$

$$\frac{di_{ds}^e}{dt} = -\gamma i_{ds}^e + \eta\beta\lambda_r + n_p \omega_r i_{qs}^e + \eta L_m \frac{{i_{qs}^e}^2}{\lambda_{dr}} + \frac{1}{\sigma L_s} v_{ds}^e \tag{22.41}$$

$$\frac{d\theta_e}{dt} = n_p \omega_r + \eta L_m \frac{i_{qs}^e}{\lambda_r} \tag{22.42}$$

where:

v_{ds}^e, v_{qs}^e: stator voltage in synchronous reference frame

i_{ds}^e, i_{qs}^e: currents in synchronous reference frame

λ_r: rotor flux in synchronous reference frame

and the expression for torque is given by:

$$T_e = \mu J \cdot \lambda_r \cdot i_{qs}^e \tag{22.43}$$

22.4.2 PARAMETER ESTIMATION

There are many parameter estimation techniques for the induction motor. Depending on the type of tests performed on the motor, the testing methods could be classified as:

Off site methods: test the motor separately from its application site [36-42]. The motor is tested individually, in the sense that it is not necessarily connected to the load it is going to drive or in the industrial setup it is going to operate in. The most common such tests are the no-load test and the locked-rotor test. The advantage of the above methods is their simplicity. However, these tests usually represent poorly the real

operating conditions of the machines (for example, they lack the effect of PWM switching on the machine parameters).

On site and off line methods: these tests are performed with the motor already connected in the industrial setup and supplied by its power converter [35,43-47]. These tests are usually meant to allow the tuning of the controller parameters to the unknown motor it supplies and are also known as self-commissioning. As they are convenient for the controller manufacturer (one control program could work for different motors), they usually are less precise than the individual tests.

On-line methods: some parameters are estimated while the motor is running on-site [48-52,55]. These methods are concerned usually with rotor parameters (L_m and R_r or the time constant, T_r) and assume that the other parameters are known. These methods usually perform well only for a good initial value of the parameter to be determined and for relatively small variations (within 10%).

The purpose of this section is the development of an induction motor model with parameters that vary as a function of operating conditions. The development is on-site and off-line. While stator resistance is measured through simple DC test, the leakage inductance, the magnetizing inductance and the rotor resistance are estimated from transient data using a constrained optimization algorithm. Through a sensitivity analysis study, for each operating condition, the parameters to which the output error is less sensitive are eliminated. The parameters are estimated under all operating conditions and mapped to them (e.g. analytical functions relating parameters to operating conditions are created). A correlation analysis is used to isolate the operating conditions that have most influence on each parameter. A core loss resistance models core losses. This resistance is estimated using a power approach and Artificial Neural Networks. No additional hardware is necessary. The same power converter and DSP board that controls the motor in the industrial setting is used to generate the signals necessary to model the motor. Therefore, phenomenon related to operation (for example PWM effects) is captured in modeling.

22.4.2.1 Estimation of stator resistance

The estimation of the stator resistance was carried out through a DC test, as shown in Figure 22.12. The resistance can be calculated as:

$$R_S = \frac{2}{3} \cdot \frac{V_a - V_c}{I_c} \tag{22.44}$$

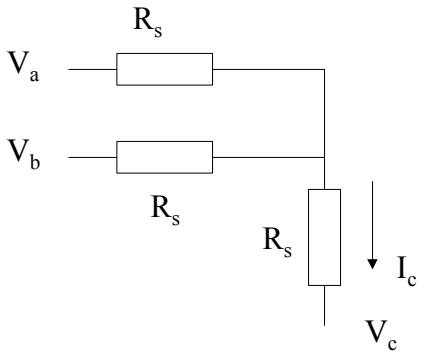

Figure 22.12 Circuit for stator resistance

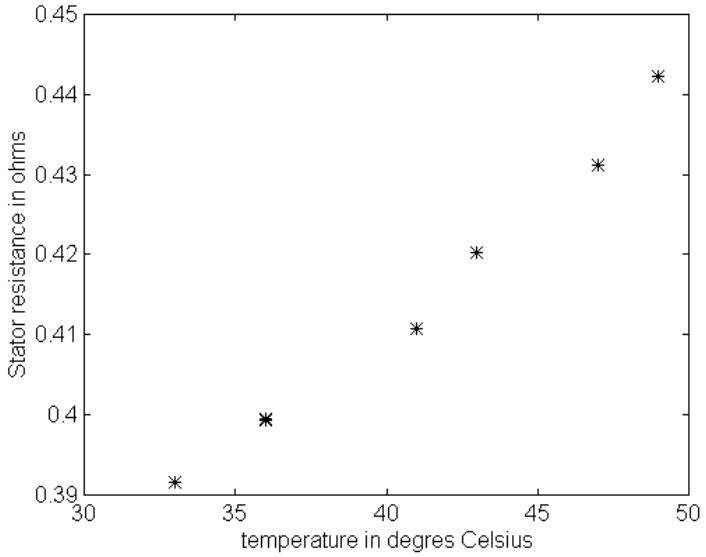

Figure 22.13 Stator resistance as a function of temperature

To capture the effect of temperature on the stator resistance, the following sequence of testing was used:

- at each test, the motor was run with an increased load;
- the stator resistance test was performed immediately after the motor stopped.

The temperature of the stator winding was also measured. The temperature dependency of the stator resistance is shown in the Figure 22.13.

22.4.2.2 Estimation of L_l, L_m, and R_r

Transient data was used to determine L_m, L_l and R_r. The data consisted in small disturbance in the steady state operation of the IM by stepping the supply voltage with 10%. The tests encompass a wide variation of frequency, supply voltage and load:

- the frequency was varied from 30 Hz to 80 Hz in steps of 10 Hz,
- the supply voltage was varied from 10% to 100% of the rated voltage value in steps of 10% for each frequency,
- the load was varied from no-load to maximum load in 8 steps.

A total of 290 data files were obtained. The estimation was performed using a constrained optimization method available in Matlab (‘constr’). Figure 22.14 shows the block diagram of the estimation procedure.

The induction motor model can be expressed in state space form as:

$$\dot{X} = AX + BU \tag{22.45}$$

and the output equation is:

$$Y = C \cdot X \tag{22.46}$$

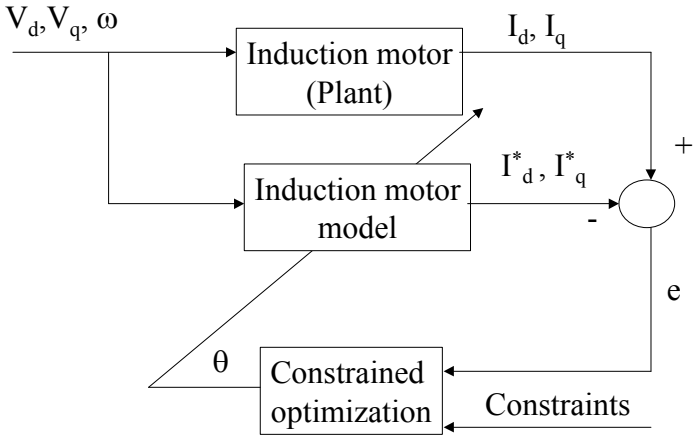

Figure 22.14 Estimation block diagram

where

$$X = \begin{bmatrix} i_{qs} & i_{ds} & \lambda_{qr} & \lambda_{dr} \end{bmatrix}^T \tag{22.47}$$

$$A = \begin{bmatrix} -\dfrac{R_s + R_r}{L_l} & 0 & \dfrac{R_r}{L_l L_m} & -\dfrac{\omega_r}{L_l} \\ 0 & -\dfrac{R_s + R_r}{L_l} & \dfrac{\omega_r}{L_l} & \dfrac{R_r}{L_l L_m} \\ -R_r & 0 & -\dfrac{R_r}{L_m} & \omega_r \\ 0 & R_r & -\omega_r & -\dfrac{R_r}{L_m} \end{bmatrix} \tag{22.48}$$

$$B = \frac{1}{L_l}\begin{bmatrix} 1 & 0 \\ 0 & 1 \\ 0 & 0 \\ 0 & 0 \end{bmatrix} \quad C = \begin{bmatrix} 1 & 0 & 0 & 0 \\ 0 & 1 & 0 & 0 \end{bmatrix} \tag{22.49}$$

and $U = \begin{bmatrix} V_q \\ V_d \end{bmatrix}$

The initial conditions for the model were established as:

$$X = \begin{bmatrix} i_{qs(0)} & i_{ds(0)} & \hat{\lambda}_{qr} & \hat{\lambda}_{rq} \end{bmatrix}^T \tag{22.50}$$

The error between model and measurements was calculated as:

$$e = \sqrt{\sum_{k=1}^{N} \left(\hat{i}_{ds(k)} - i_{ds(k)}\right)^2 + \left(\hat{i}_{qs(k)} - i_{qs(k)}\right)^2} \tag{22.51}$$

where ^ - estimated values

The constrained optimization function is used to minimize the error function by modifying the parameter vector, :

$$\theta = \begin{bmatrix} L_m & R_r & L_l & \hat{\lambda}_{qr(0)} & \hat{\lambda}_{dr(0)} \end{bmatrix} \tag{22.52}$$

The values of stator resistance were based on temperature measurements. The initial values of the fluxes are not normally included in the parameter vector since they can be calculated from the initial conditions of the currents at steady state. However, these currents are noise corrupted and their measurement error will propagate into the calculation of the initial values of the flux. Furthermore, since flux equations have a large time constant, the initial condition error would influence the flux observation over the entire transient measurement (the self-correction of an otherwise convergent flux observer [57] will not have the time to correct the initial condition error) and will yield erroneous parameter estimates.

The authors observed that the parameter vector modification increased the rate of convergence of the algorithm. Constraints on R_r, L_l, and Lm were imposed as 10% of the rated value for the lower bound and 300% for the upper bound. For $\lambda_{d(0)}$ and $\lambda_{d(0)}$ the constraints were imposed as +/_ 200% of the saturation value (0.5 Wb).

22.3.3 SENSITIVITY ANALYSIS

Since an output error estimation method is used, there is no theoretical guarantee that the parameters will converge to their actual values. Therefore it is necessary to study the effect of each parameter on the total error. It is obvious that those parameters with little effect on the total error will be more prone to estimation errors than parameters that affect it more. For any data point, the error can be expressed as:

$$E(t) = I \cdot \sin(\omega t + \varphi) - \hat{I} \cdot \sin(\omega t + \hat{\varphi}) \tag{22.53}$$

At steady state, the squared error per period is:

$$e^2 = \frac{1}{T}\int_0^T E^2(t)dt = \frac{1}{2}\left(I^2 + \hat{I}^2 - 2\hat{I} \cdot I\cos(\varphi - \hat{\varphi})\right) \tag{22.54}$$

The sensitivity of the squared error to a parameter (y) can be expressed as:

$$S_y^e = \frac{e^2(\hat{I}(y + \Delta y), I(y))}{\Delta y} \cdot \frac{y}{I} \tag{22.55}$$

For the proposed model, the steady state current (complex form) can be expressed as:

$$\vec{I} = V \cdot \frac{\frac{R_r}{s} + jX_m}{-X_l X_m + \frac{R_s R_r}{s} + j\left(\frac{R_r}{s}(X_l + X_m) + R_s X_m\right)} \tag{22.56}$$

and I and φ are the module and phase angle of $\vec{I}$.

The sensitivity analysis was conducted for a slip ranging from 0 to 10% (larger values of s are unobtainable at steady state) and a frequency from 20 Hz to 100Hz. The rated values of

the parameters were used. Figure 15 shows a comparison of sensitivity for R_r, L_m and L_l at 60 Hz. Figure 22.16-22.18 represent the sensitivity of each individual parameter for different frequencies and slips. It can be seen that the sensitivity of the error to L_l or R_r is low at low slip. Large errors can be introduced at low slip since their effect on the error is small. A limit of 2% on the slip was imposed on the slip values. The L_l and R_r estimates below this value are discarded. For large values of the slip the sensitivity of the error to L_m decreases to 0. L_m estimates for slip values larger than 2% were discarded.

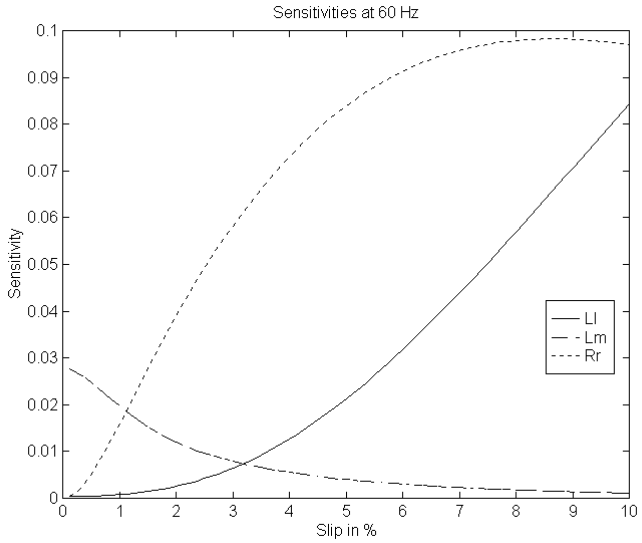

Figure 22.15 Sensitivity of error to parameters as a function of slip at 60 Hz

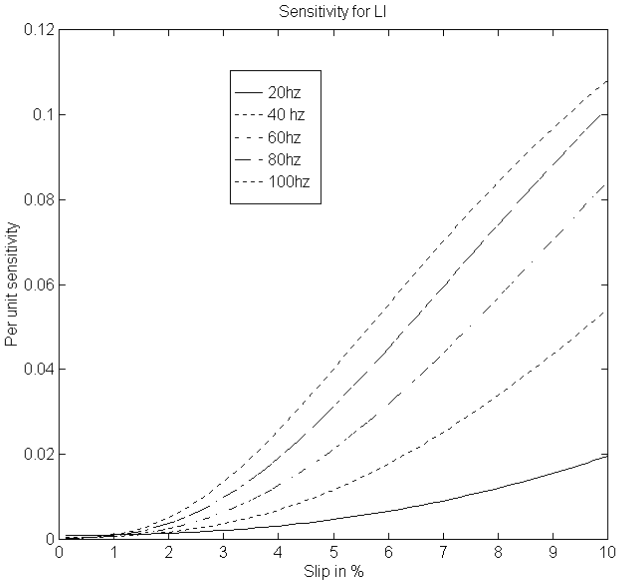

Figure 22.16 Sensitivity of error to L_l as a function of slip at different frequencies

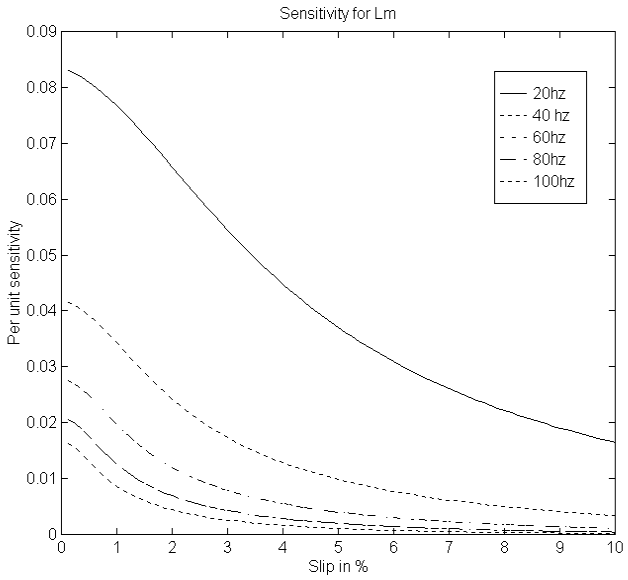

Figure 22.17 Sensitivity of error to L_m as a function of slip at different frequencies

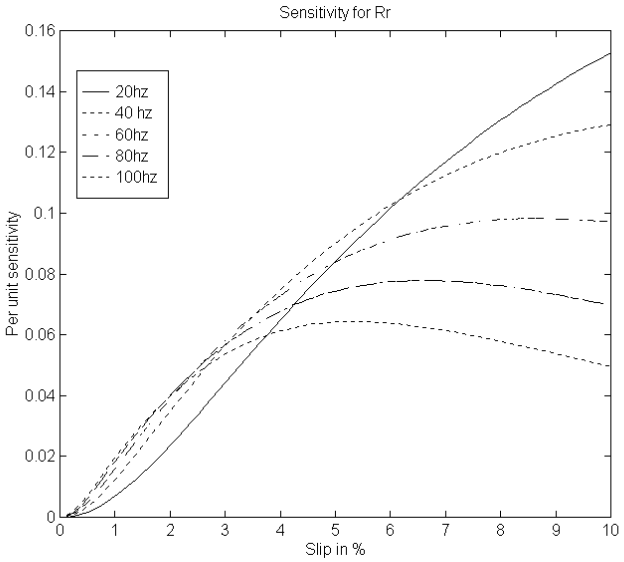

Figure 22.18 Sensitivity of error to R_r as a function of slip at different frequencies

Observation

The concept of sensitivity of the currents (error) to the parameters can be extended to more classical induction motor tests: in the no-load test, only L_m is estimated whereas in the locked rotor test R_r and L_l are estimated.

22.4.4 PARAMETER MAPPING TO OPERATING CONDITIONS

The model proposed here is dependent on the operating conditions. Up to this point, the parameters of the motor were estimated for various operating conditions. The purpose of this

Table 22.10 Correlation between parameters and operating conditions

Parameter	i_{ds}^e	i_{qs}^e	*Is*	Ws
L_m	-0.9287	0.0167	-0.6652	0.3473
R_r	0.1543	0.8061	0.8023	0.5485
L_l	-0.3212	-0.4264	-0.7135	0.0177

section is to find the relation of the parameters to the operating conditions in a form that allows for use in a control environment. However, in order to be able to define an operating condition or to relate (map) a parameter to a condition, a correlation analysis is necessary. This establishes the "strong" and "weak" dependencies of parameters to operating variables. The variables for the correlation study are selected intuitively as:

i_{ds}^e, i_{qs}^e – the stator currents in synchronous reference frame
Is – the stator current (peak value)
w_s- slip frequency

It could be argued that temperature is also a factor in this mapping. However, since the only temperature measurement available was the stator temperature (and was used for stator resistance calculation) it was not used in this correlation study. The correlation between two variables (in this case one variable is a parameter (y) and the other a operating condition variable (x)) can be defined as:

$$C_{x,y} = \frac{\frac{1}{N-1}\sum_{k=1}^{N}\left((x_k - \bar{x})(y_k - \bar{y})\right)}{\sigma_x \sigma_y} \tag{22.57}$$

where $\bar{x}, \bar{y}$ are the mean of x and y respectively and σ_x, σ_y are their standard deviations. Table 10 shows the results of the correlation:

Mapping consists in expressing the parameters of the motor as analytical functions of the operating conditions. The selection of the variables describing the operating conditions is based on the correlation study.

22.4.4.1 Magnetizing inductance, L_m

A strong correlation was observed between L_m and i_{ds}^e. L_m clearly saturates with an increase in i_{ds}^e. A second order polynomial was used to represent the dependency of L_m to i_{ds}^e in the saturated region.

$$L_m(i_{ds}^e) = k_1 \cdot {i_{ds}^e}^2 + k_2 \cdot i_{ds}^e + k_3 \tag{22.58}$$

Figure 22.19 shows a comparison between the polynomial and the results of the estimation.

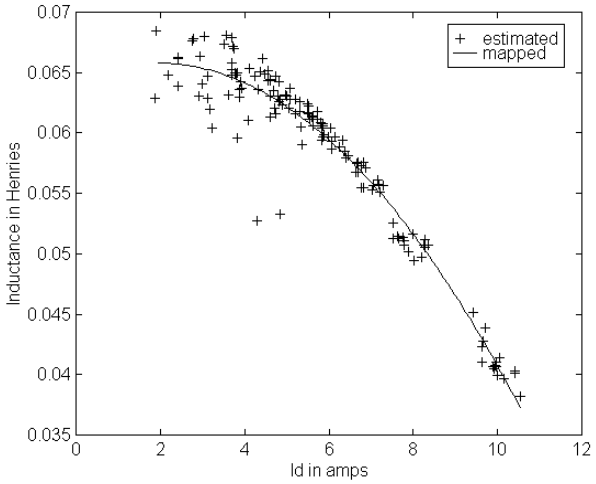

Figure 22.19 L_m as function of i_{ds}^e

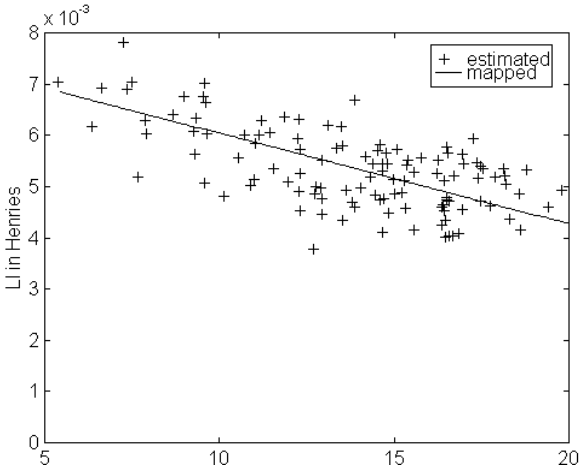

Figure 22.20 L_l as function of *Is*

22.4.4.2 Leakage inductance, L_l

A strong correlation was also observed between L_l and *Is*. L_l saturates with an increase in *Is*. A linear approximation was used to represent the dependency of L_l to *Is* and is shown in Figure 22.20.

$$L_l(I_s) = k_4 \cdot I_s + k_5 \tag{22.59}$$

22.4.4.3 Rotor resistance, R_r

It can be safely assumed that the rotor resistance varies as a function of two factors: slip frequency (through skin effect) and rotor temperature (immeasurable). However, Table 10 shows a correlation between R_r and *ws* but also i_{qs}^e. The correlation is shown in Figure 22.21.

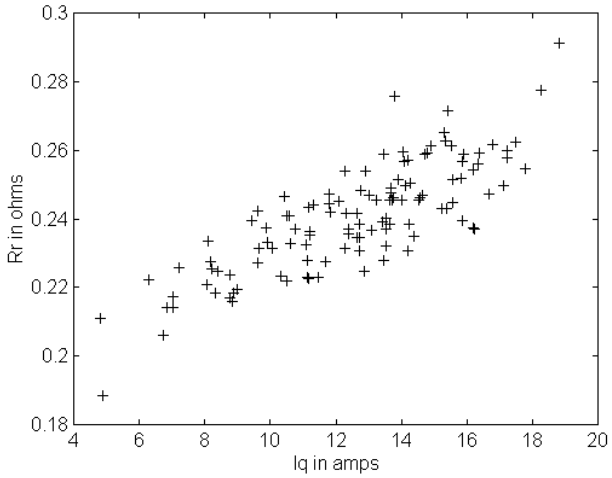

Figure 22.21 R_r as function of i_{qs}^e

The correlation is due to the fact that both slip frequency and temperature are proportional to i_{qs}^e. It was observed that the $R_r(i_{qs}^e)$ correlation holds only if the motor runs for a few minutes at a certain operating condition, to allow for temperature to reach a steady state. A sudden variation in i_{qs}^e would not determine a sudden change in R_r if slip frequency remains constant since temperature does not change as fast. Therefore, the $R_r(i_{qs}^e)$ relation can only be used at steady state.

In order to establish the influence of slip frequency on R_r, a test similar to a locked rotor was used. The difference was that the rotor was not mechanically locked, but the voltages were small enough that the rotor would not move. The frequency was varied between 5 Hz and 120 Hz (1 Hz increments in the 5-10 Hz region and 10 Hz increments for the rest). Prior to each series of tests, the motor was run under a loading condition (no-load, medium load and full load) to assure heating of the rotor. A temperature sensor was mounted on the stator. This sensor was used for an indication when temperature has reached a steady state (for each

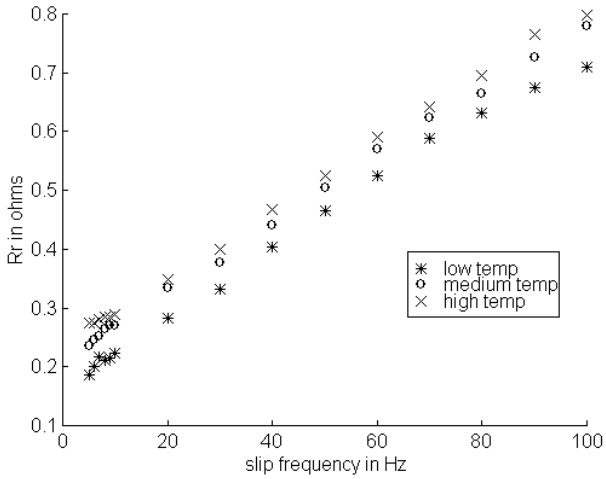

Figure 22.22 Rotor resistance as function of slip frequency for different temperatures

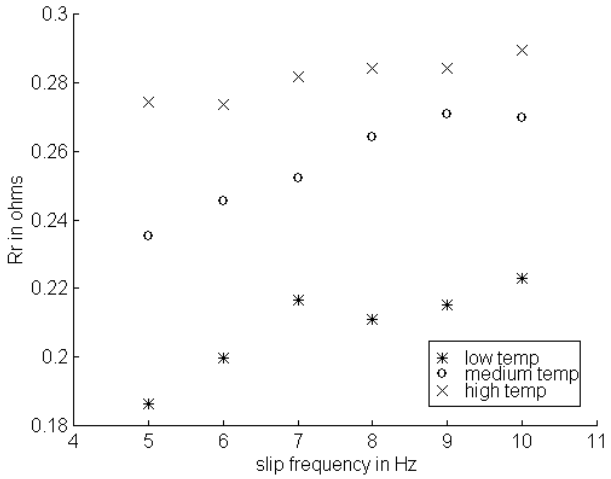

Figure 22.23 Rotor resistance as function of slip frequency for lower frequencies

loading condition). Figure 22.22 shows the results of the R_r estimation as a function of slip frequency (for locked rotor, equal to stator frequency). Figure 22.23 shows just the 5-10 Hz region, which is of more interest for us, since slip rarely exceeds this range.

Observation 1. Since rotor frequency (slip frequency) influences the values of rotor resistance, the locked rotor test must be carried out at a low frequency if the rated value of rotor resistance is sought. This is particularly important for squirrel-cage motors in which skin effect is present. For example, for the motor used in this research, a locked rotor test at rated frequency would yield a value of rotor resistance approximately 3 times higher than real. Since rotor temperature measurements are hardly possible, a precise off-line mapping of rotor resistance to operating conditions is impossible. However, due to the linearity (within the range of interest) of the relation between rotor resistance and slip frequency, an on-line observer can be developed.

The observer is based on the assumptions that the rotor temperature varies much slower than the other variables (current, speed etc) and that steady state operating conditions exist (e.g. the motor is not in continuous transient). The rotor resistance dependency to slip frequency and rotor temperature can be expressed as:

$$R_r(\omega_s, T) = R_1(T) + k_6 \cdot \omega_s \tag{22.60}$$

in which $R_1(T)$ is the influence of temperature (unknown). The coefficient k6 (influence of slip frequency) can be estimated off line from the locked rotor tests measurements. At each operating condition (steady state), the value of rotor resistance and slip frequency can be estimated with an observer, as shown in the next section). Then for each loading condition (temperature):

$$\hat{R}_1(T) = \hat{R}_r(\omega_s, T) - k_6 \cdot \hat{\omega}_s \tag{22.61}$$

Assuming that temperature changes slowly, at each instant of time, knowing the slip frequency allows for the determination of rotor resistance. Each time a steady state condition is detected, $R_1(T)$ is re-evaluated and rotor resistance calculated as function of slip frequency.

Observation 2. It can be argued that since rotor resistance is estimated, there is no need in determining $R_1(T)$. This is true while the motor operates at steady state. However, for efficiency optimization it is important to predict the variation of rotor resistance prior to a new steady state condition. For this case it is important to have the value of $R_1(T)$ and predict the variation of R_r based on slip frequency.

22.4.5 CORE LOSS ESTIMATION

One should note that since the slip is non-zero for the no-load test and R_r is already known, R_c could be theoretically calculated from the parallel resistance of R_r and R_c. However, even for most precise speed encoders, the error in calculating a slip approaching zero could translate in an order of magnitude of error when calculating R_r /s (s being the slip $s = \omega_s / \omega_e$).

A power-based approach is used for calculating the core resistance.

22.4.5.1 Calculation of rotor losses at frequencies of interest

Use the no-load tests and calculate the rotor power losses for each data set:

$$P_{rotor} = V_s I_s \cos(\varphi) - R_s I_s^2 \tag{22.62}$$

A plot of these losses is shown in Figure 24 for various frequencies. The losses increase with both the frequency and the rotor flux.

22.4.5.2 Calculation of friction and windage losses using ANN

Since core losses are zero when flux is zero, the intersection of the power curves with the vertical axis determines the friction and windage losses for a specific frequency. To find the friction and windage losses for all frequencies, an ANN was used to map the rotor losses to frequency and flux. Multi-layer feed-forward neural networks have often been used in system identification studies. These networks consist of a number of basic computational units called processing elements connected together to form multiple layers. A typical processing element forms a weighted sum of its inputs and passes the result through a non-linear transformation

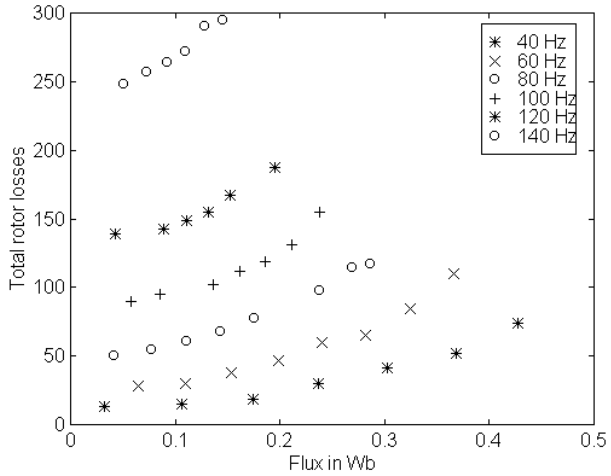

Figure 22.24 Rotor power losses for no-load test

(also called transfer function) to the output. The transfer function may also be linear in which case the weighted sum is propagated directly to the output path. The ANN used in this research consists of processing elements arranged in three distinct layers. Data presented at the network input layer are processed and propagated through a hidden layer, to the output layer. Training a network is the process of iteratively modifying the strengths (weights) of the connecting links between processing elements as patterns of inputs and corresponding desired outputs are presented to the network.

In this work, the mathematical relationship between the input and output patterns can be described as:

$$P_{rotor\_losses} = N_d(\lambda, \omega_e) \tag{22.63}$$

where N_d is a non-linear neural network mapping to be established. The ANN used in this study is shown in Figure 22.25 and consists of 2 processing elements in the input layer, corresponding to each variable. A single processing element in the output layer corresponds to the losses being modeled. The number of elements in the hidden layer is arbitrarily chosen depending on the complexity of the mapping to be learned. A hyperbolic tangent (tanh) transfer function is used in all hidden layer elements, while all elements in the input layer and output layer have linear (1:1) transformations.

The back-propagation algorithm is used to train the neural network such that the sum squared error, E, between actual network outputs, O, and corresponding desired outputs, ζ, is minimized over all training patterns μ

$$E = \sum_{\mu}[\zeta_\mu - O_\mu]^2 \tag{22.64}$$

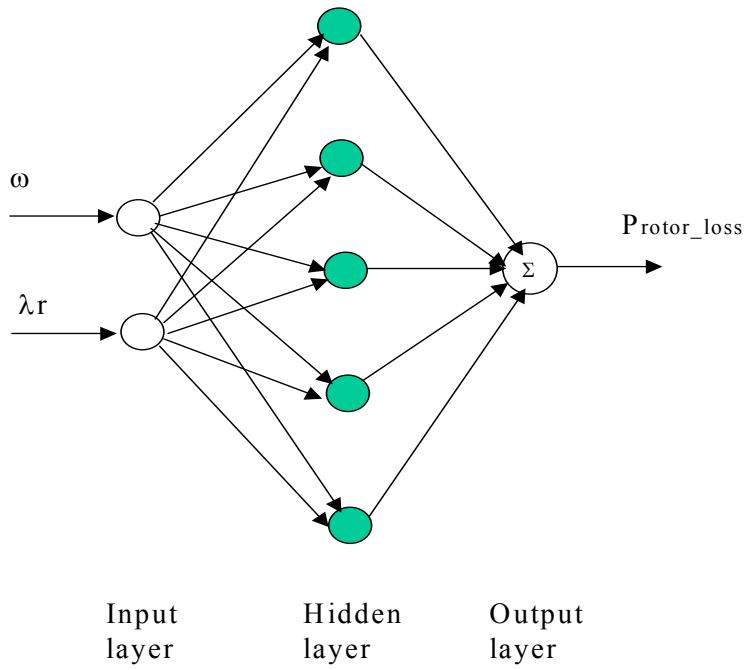

Figure 22.25 ANN Model for P_{rotor_losses}

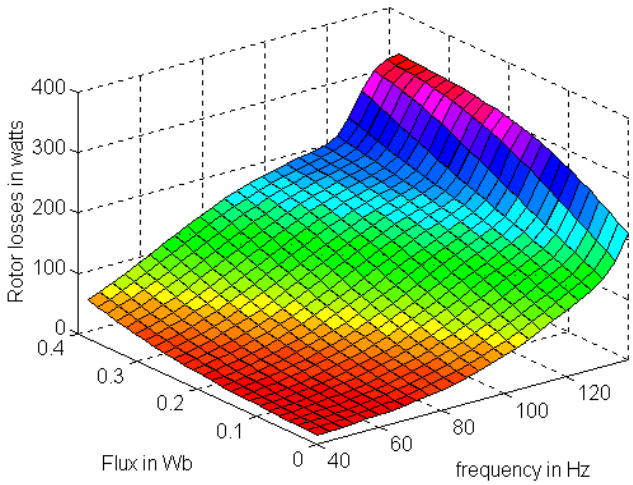

Figure 22.26 Mapping of rotor losses using ANN

After estimating the non-linear mapping N_d in terms of the neural network, the network output P_{rotor_losses} is computed from the 2x1 input vector P according to the following equation:

$$P_{rotor\_losses} = W_2 \cdot \tanh(W_1 \cdot P + B_1) + B_2 \tag{22.65}$$

W_2 denotes the matrix of connecting weights from the hidden layer to the output layer. W_1 is the weight matrix from the input-layer to the hidden-layer. If there are m processing elements in the hidden layer, W_2 is of size 1xm, and W_1 is of size mx1. Bias terms B_2 and B_1 are used as connection weights from an input with a constant value of one. B_2 and B_1 denote the 1x1 and mx1 bias vectors from the bias to the output-layer, and from the bias to the hidden-layer respectively. The task of training is to determine the matrices W_1, W_2, and bias vectors B_1, B_2. The training patterns for the neural network models are composed of the no-load test data. Each data set is a vector of λ, ω_e and P_{rotor_losses}. The results of the mapping are shown in Figure 22.26. Friction and windage losses can be calculated for ANN at zero flux.

22.4.5.3 Calculation of core losses

Core losses for each frequency and flux can be determined by subtracting the friction and windage losses and the resistive rotor losses from the rotor losses.

$$P_{core}(\omega, \lambda_r) = P_{rotor\_losses}(\omega, \lambda_r) - P_{f\&w}(\omega_r) - R_r I_{r2}^2 \tag{22.66}$$

where

$$P_{f\&w} = R_r \frac{1-s}{s} I_{r2}^2 = P_{rotor\_losses}(\omega, 0) = N_d(\omega, 0) \tag{22.67}$$

Since

$$P_{f\&w} = R_r \frac{1-s}{s} I_{r2}^2 >> R_r I_{r2}^2,$$

the last term of the previous equation is neglected.

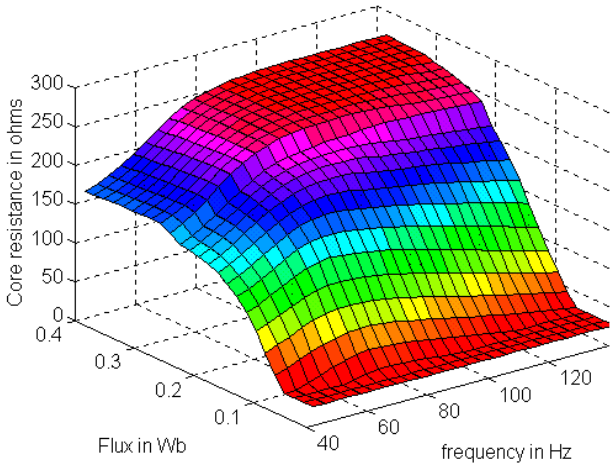

Figure 22.27 Rotor core losses as function of flux and frequency

22.4.5.4 Calculation of core resistance

For each data point, calculate the core loss resistance as:

$$R_c(\omega_e, \lambda_r) = \frac{P^2_{rotor\_losses}(\omega_e, \lambda_r)}{I_r^2 \cdot P_{core}(\omega_e, \lambda_r)} \tag{22.68}$$

Map the core loss resistance to flux and frequency using ANN. The procedure is similar to the rotor loss mapping. Figure 27 presents the results of the mapping.

22.4.6 Model Validation

22.4.6.1 Steady state- power input

In order to validate the model at steady state, tests encompassing the entire range of operation of the induction motor were used. The frequency of the motor was varied from 30 to 70 Hz. The supply voltage was varied from 10% to 100% of rated. For each voltage and frequency entry, the load was varied from zero to maximum value. For all data sets, input power was measured and compared to the input power calculated using measured voltage and speed and the model. Figure 22.28 shows the results of the comparison.

22.4.6.2 Dynamic

The model was used to predict the transient performance after an input voltage disturbance. Figures 22.29-22.31 present the results in terms of the stationary reference frame currents. The measured and estimated currents are represented on the same graph (measured – solid line and estimated -dotted line).

A second type of tests consisted in transient behavior when starting the motor. The start-up currents (measured and simulated) are shown in Figures 22.32-22.33 in synchronous reference frame. Figure 22.32 represents the results when variable parameters were used; whereas Figure 22.33 represents the results when rated (fixed) parameters were used.

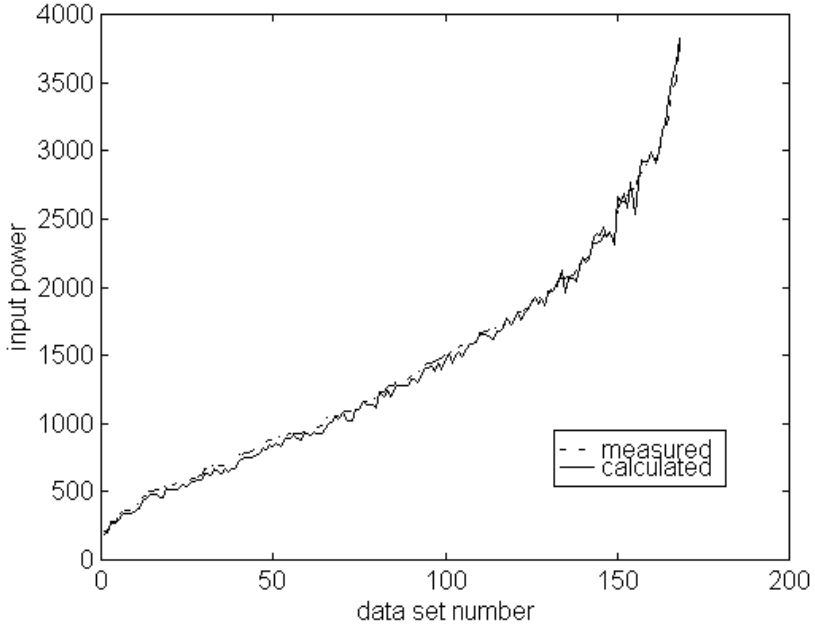

Figure 22.28 Measured and calculated input power

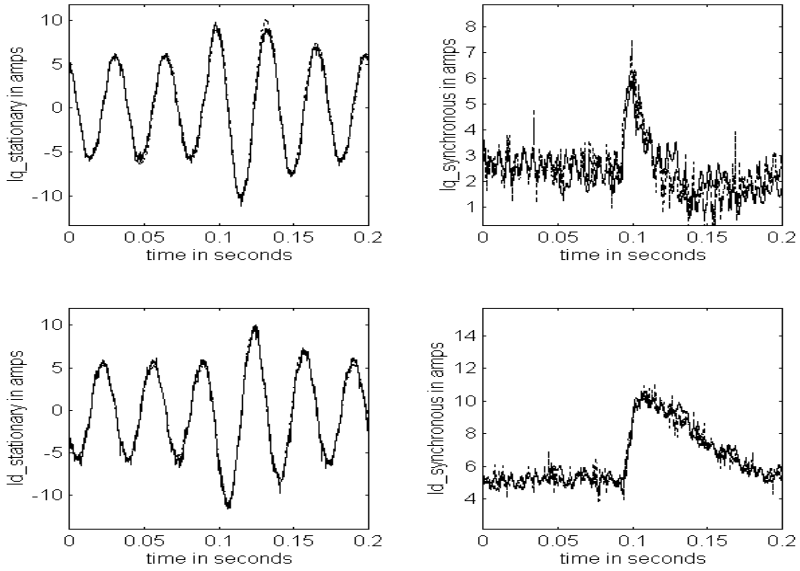

Figure 22.29 Model validation for large disturbance test at low frequency

22.4.7 CONCLUSIONS

A systematic procedure for induction motor modeling was developed in this chapter. The model includes the effects of inductance saturation (both for magnetizing and leakage inductance) and the effects of the core losses. It is also shown that there is a variation of rotor resistance as a function of slip frequency. The leakage inductance, magnetizing inductance and rotor resistance are estimated from transient data information using a constrained optimization method. Sensitivity analysis is employed to show that error sensitivity to

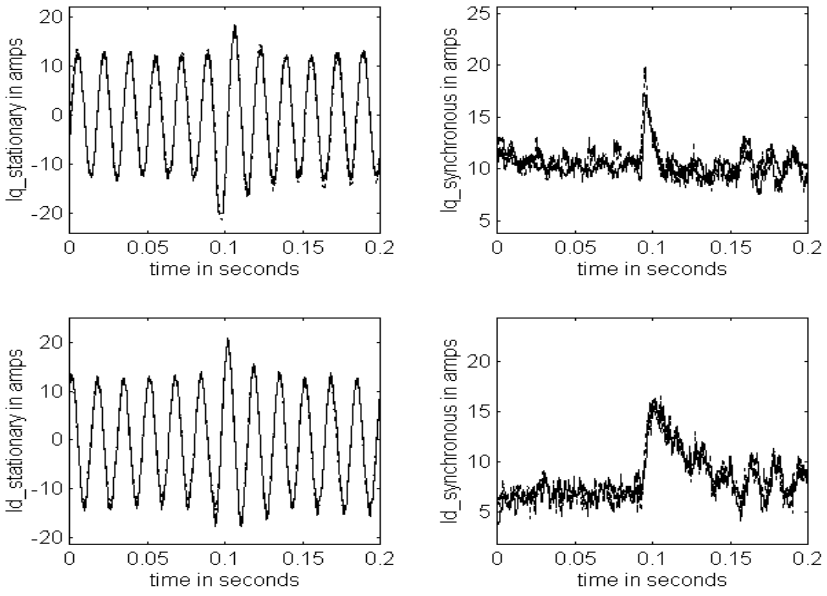

Figure 22.30 Model validation for large disturbance test at medium frequency

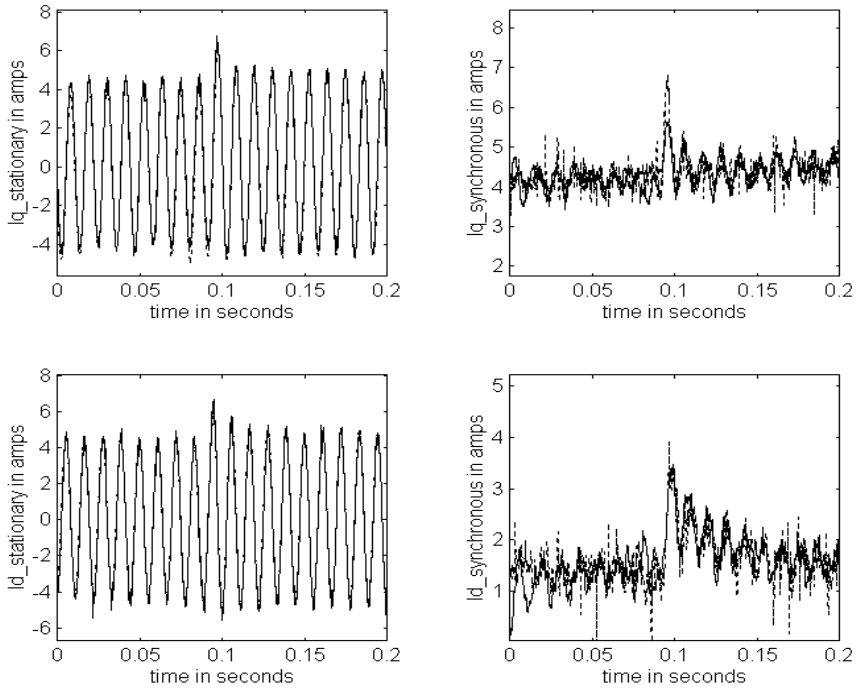

Figure 22.31 Model validation for large disturbance test at high frequency

parameters varies as a function of slip. The analysis eliminates parameters with that yield low sensitivity. Analytical functions are used to map the parameters to operating conditions. Core losses are estimated using a power approach. ANN are used to map the total rotor losses (iron

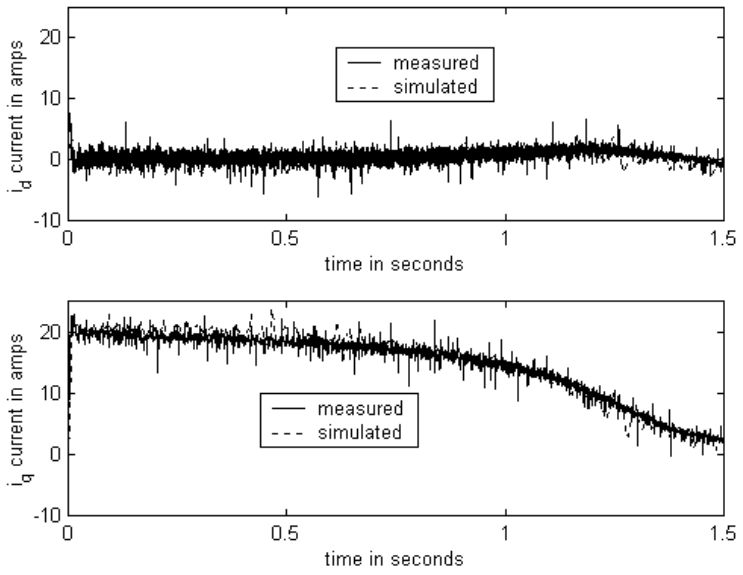

Figure 22.32 Transient response for start-up from zero speed

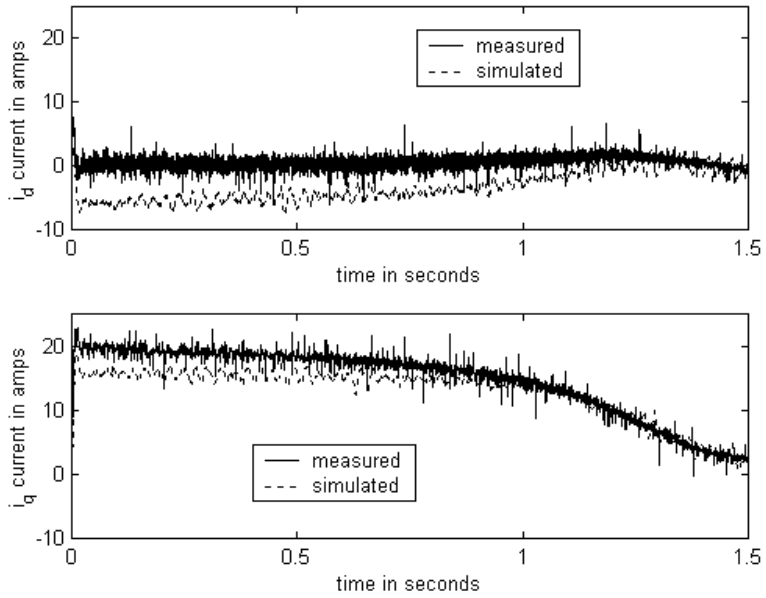

Figure 22.33 Transient response for start-up from zero speed with rated fixed parameters

losses, friction and windage losses) to flux and frequency. The core losses are obtained by subtracting the rotor losses at zero flux (generated by the ANN) from the rotor loss surface. The model is validated using tests covering various operating conditions. For steady-state validation, the model is shown to correctly predict the power input of the motor. For dynamic validation, input voltage disturbance tests and start-from-zero tests were employed. The model correctly predicted both tests.

22.5 MODELING AND PARAMETER IDENTIFICATION OF SWITCHED RELUCTANCE MACHINES

22.5.1 INTRODUCTION

Switched reluctance machines (SRM) have undergone rapid development in hybrid electric vehicles and other automotive applications over the last two decades. This is mainly due to the various advantages of SRMs over the other electric machines, such as simple and robust construction, and fault-tolerant performance.

In most of these applications, speed and torque control are necessary. To obtain high quality control, a proper model of SRM is often needed. At the same time, to increase reliability and reduce cost, sensorless controllers (without rotor position/speed sensors) are preferred. With the rapid progress in microprocessors (DSP), MIPS (Million Instructions Per Second) - intensive control techniques such as sliding mode observers and controllers [57] become more and more promising. An accurate nonlinear model of the SRM is essential to realize such control algorithms.

The nonlinear nature of SRM and high saturation of phase winding during operation makes the modeling of SRM a challenging work. The flux linkage and phase inductance of SRM change with both the rotor position and the phase current. Therefore the nonlinear model of SRM must be identified as a function of the phase current and rotor position. Two main models of SRM have been suggested in the literature – the flux model [58] and the inductance model [59]. In the latter one, "the position dependency of the phase inductance is represented by a limited number of Fourier series terms and the nonlinear variation of the inductance with current is expressed by means of polynomial functions" [59]. This model can describe the nonlinearity of SRM inductance quite well. We will use this model here.

Once a model is selected, how to identify the parameters in the model becomes an important issue. Finite element analysis can provide a model that will be subjected to substantial variation after the machine is constructed with manufacturing tolerances. Therefore, the model and parameters need to be identified from test data. As a first step, the machine model can be estimated from standstill test using output error estimation (OE) or maximum likelihood estimation (MLE) techniques. This method has already been applied successfully to identify the model and parameters of induction and synchronous machines.

Furthermore, during online operation, the model structures and parameters of SRMs may differ from the standstill ones because of saturation and losses, especially at high current. To model this effect, a damper winding may be added into the model structure, which is in parallel with the magnetizing winding. The magnetizing current and damper current are highly nonlinear functions of phase voltage, rotor position, and rotor speed. They are not measurable during operation, and are hard to be expressed with analytical functions. Neural network mapping are usually good choices for such tasks [62-64]. A 2-layer recurrent neural network has been adopted here to estimate these two currents, which takes the phase voltage, phase current, rotor position and rotor speed as inputs. When the damper current is estimated and damper voltage is computed, the damper parameters can be identified using output error or maximum likelihood estimation techniques.

In this section, the procedures to identify an 8/6 SRM parameters from standstill test data are presented after an introduction to the inductance model of SRM. Then a 2-layer recurrent neural network is constructed, trained and applied to identify the damper parameters of SRM from operating data. Model validation through online test is also given, which proves the applicability of the proposed methods.

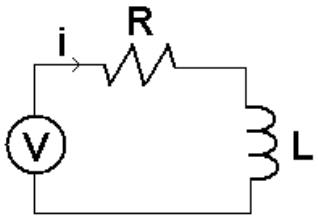

Figure 22.34 Inductance model of SRM at standstill

22.5.2 INDUCTANCE MODEL OF SRM AT STANDSTILL

The inductance model of switched reluctance motor is shown in Figure 34. The phase winding is model as a resistance (R) in series of an inductance (L).

Since the phase inductance changes periodically with the rotor position angle, it can be expressed as a Fourier series with respect to rotor position angle θ:

$$L(\theta,i)=\sum_{k=0}^{m}L_k(i)\cos kN_r\theta\,, \tag{2269}$$

where Nr is the number of rotor poles, and m is the number of terms included in the Fourier series. High order terms (H.O.T.) can be omitted without bringing significant errors.

In [59], The authors suggest using the first three terms of the Fourier series (m=3), but more terms can be added to meet accuracy requirements.

To determine the coefficients $L_k(i)$ in the Fourier series, we need to know the inductances at several specific positions. Use $L_\theta(i)$ to represent the inductance at position θ, which is a function of phase current i and can be approximated by a polynomial:

$$L_\theta(i)=\sum_{n=0}^{k}a_{\theta,n}i^n\ . \tag{22.70}$$

where k is the order of the polynomial and $a_{\theta,n}$ are the coefficients of polynomial. In our research, $k = 5$.

For an 8/6 machine, Nr=6. When θ=0 is chosen at the aligned position of phase A, then θ=30 is the unaligned position of phase A. Usually the inductance at unaligned position can be treated as a constant.

$$L_{30^0}=const \tag{22.71}$$

22.5.2.1 Three-term inductance model

If three terms are used in the Fourier series (m=3), then we can compute the three coefficients L_0 , L_1 , and L_2 from L_{0^0} (aligned position), L_{15^0} (midway position), and L_{30^0} (unaligned position). Since

$$\begin{bmatrix}L_{0^0}\\L_{15^0}\\L_{30^0}\end{bmatrix}=\begin{bmatrix}1&1&1\\1&\cos(6*15^0)&\cos(12*15^0)\\1&\cos(6*30^0)&\cos(12*30^0)\end{bmatrix}\begin{bmatrix}L_0\\L_1\\L_2\end{bmatrix}=\begin{bmatrix}1&1&1\\1&0&-1\\1&-1&1\end{bmatrix}\begin{bmatrix}L_0\\L_1\\L_2\end{bmatrix}, \tag{22.72}$$

so

$$\begin{bmatrix} L_0 \\ L_1 \\ L_2 \end{bmatrix} = \begin{bmatrix} 1 & 1 & 1 \\ 1 & 0 & -1 \\ 1 & -1 & 1 \end{bmatrix}^{-1} \begin{bmatrix} L_{0^0} \\ L_{15^0} \\ L_{30^0} \end{bmatrix} = \begin{bmatrix} 1/4 & 1/2 & 1/4 \\ 1/2 & 0 & -1/2 \\ 1/4 & -1/2 & 1/4 \end{bmatrix} \begin{bmatrix} L_{0^0} \\ L_{15^0} \\ L_{30^0} \end{bmatrix}. \tag{22.73}$$

Or in separate form:

$$L_0 = \frac{1}{2}[\frac{1}{2}(L_{0^0} + L_{30^0}) + L_{15^0}],$$

$$L_1 = \frac{1}{2}(L_{0^0} - L_{30^0}), \tag{22.74}$$

$$L_2 = \frac{1}{2}[\frac{1}{2}(L_{0^0} + L_{30^0}) - L_{15^0}].$$

22.5.2.2 Four-term inductance model

If Four terms are used in the Fourier series (m=4), then we can compute the four coefficients L_0, L_1, L_2, and L_3 from L_{0^0} (aligned position), L_{10^0}, L_{20^0}, and L_{30^0} (unaligned position). Since

$$\begin{bmatrix} L_{0^0} \\ L_{10^0} \\ L_{20^0} \\ L_{30^0} \end{bmatrix} = \begin{bmatrix} 1 & 1 & 1 & 1 \\ 1 & \cos(6*10^0) & \cos(12*10^0) & \cos(18*10^0) \\ 1 & \cos(6*20^0) & \cos(12*20^0) & \cos(18*20^0) \\ 1 & \cos(6*30^0) & \cos(12*30^0) & \cos(18*30^0) \end{bmatrix} \begin{bmatrix} L_0 \\ L_1 \\ L_2 \\ L_3 \end{bmatrix}, \tag{22.75}$$

so

$$\begin{bmatrix} L_0 \\ L_1 \\ L_2 \\ L_3 \end{bmatrix} = \begin{bmatrix} 1/6 & 1/3 & 1/3 & 1/6 \\ 1/3 & 1/3 & -1/3 & -1/3 \\ 1/3 & -1/3 & -1/3 & 1/3 \\ 1/6 & -1/3 & 1/3 & -1/6 \end{bmatrix} \begin{bmatrix} L_{0^0} \\ L_{10^0} \\ L_{20^0} \\ L_{30^0} \end{bmatrix}. \tag{22.76}$$

Or in separate form:

$$L_0 = \frac{1}{3}[\frac{1}{2}(L_{0^0} + L_{30^0}) + (L_{10^0} + L_{20^0})],$$

$$L_1 = \frac{1}{3}(L_{0^0} + L_{10^0} - L_{20^0} - L_{30^0}), \tag{22.77}$$

$$L_2 = \frac{1}{3}(L_{0^0} - L_{10^0} - L_{20^0} + L_{30^0})$$

$$L_3 = \frac{1}{3}[\frac{1}{2}(L_{0^0} - L_{30^0}) - (L_{10^0} - L_{20^0})].$$

22.5.2.3 Five-term inductance model

If Five terms are used in the Fourier series (m=5), then we can compute the five coefficients L_0, L_1, L_2, L_3, and L_4 from L_{0^0} (aligned position), $L_{7.5^0}$, L_{15^0} (midway position), $L_{22.5^0}$, and L_{30^0} (aligned position). Since

$$\begin{bmatrix} L_{0^0} \\ L_{7.5^0} \\ L_{15^0} \\ L_{22.5^0} \\ L_{30^0} \end{bmatrix} = \begin{bmatrix} 1 & 1 & 1 & 1 & 1 \\ 1 & \cos(6*7.5^0) & \cos(12*7.5^0) & \cos(18*7.5^0) & \cos(24*7.5^0) \\ 1 & \cos(6*15^0) & \cos(12*15^0) & \cos(18*15^0) & \cos(24*15^0) \\ 1 & \cos(6*22.5^0) & \cos(12*22.5^0) & \cos(18*22.5^0) & \cos(24*22.5^0) \\ 1 & \cos(6*30^0) & \cos(12*30^0) & \cos(18*30^0) & \cos(24*30^0) \end{bmatrix} \begin{bmatrix} L_0 \\ L_1 \\ L_2 \\ L_3 \\ L_4 \end{bmatrix}, \tag{22.78}$$

so

$$\begin{bmatrix} L_0 \\ L_1 \\ L_2 \\ L_3 \\ L_4 \end{bmatrix} = \begin{bmatrix} 1/8 & 1/4 & 1/4 & 1/4 & 1/8 \\ 1/4 & \sqrt{2}/4 & 0 & -\sqrt{2}/4 & 1/4 \\ 1/4 & 0 & -1/2 & 0 & 1/4 \\ 1/4 & -\sqrt{2}/4 & 0 & \sqrt{2}/4 & 1/4 \\ 1/8 & -1/4 & 1/4 & -1/4 & 1/8 \end{bmatrix} \begin{bmatrix} L_{0^0} \\ L_{7.5^0} \\ L_{15^0} \\ L_{22.5^0} \\ L_{30^0} \end{bmatrix}. \tag{22.79}$$

Or in separate form:

$$L_0 = \frac{1}{4}[\frac{1}{2}(L_{0^0} + L_{30^0}) + (L_{7.5^0} + L_{15^0} + L_{22.5^0})],$$

$$L_1 = \frac{1}{4}[(L_{0^0} + L_{30^0}) + \sqrt{2}(L_{7.5^0} - L_{22.5^0})]$$

$$L_2 = \frac{1}{4}(L_{0^0} - 2L_{15^0} + L_{30^0}), \tag{22.80}$$

$$L_3 = \frac{1}{4}[(L_{0^0} - L_{30^0}) - \sqrt{2}(L_{7.5^0} - L_{22.5^0})]$$

$$L_4 = \frac{1}{4}[\frac{1}{2}(L_{0^0} + L_{30^0}) - (L_{7.5^0} - L_{15^0} + L_{22.5^0})].$$

22.5.2.4 Voltages and Torque Computation

Besides inductance, the phase winding also contains resistance (R). A simple model structure of phase winding is shown in Figure 22.34.

Based on the inductance model described above, the phase voltage equations can be formed and the electromagnetic torque can be computed from the partial derivative of magnetic co-energy with respect to rotor angle θ. They are listed here:

$$\begin{aligned} V &= R \cdot i + L\frac{di}{dt} + i\frac{dL}{dt} \\ &= R \cdot i + L\frac{di}{dt} + i(\frac{\partial L}{\partial \theta}\omega + \frac{\partial L}{\partial i}\frac{di}{dt}) \end{aligned}, \tag{22.81}$$

where

$$\frac{\partial L}{\partial i} = \sum_{k=0}^{m} \frac{\partial L_k(i)}{\partial i} \cos kN_r\theta \tag{22.82}$$

$$\frac{\partial L}{\partial \theta} = -\sum_{k=0}^{m} L_k(i) kN_r \sin kN_r\theta \,. \tag{22.83}$$

And

$$\begin{aligned} T &= \frac{\partial W_c(\theta, i)}{\partial \theta} = \frac{\partial\{\int [L(\theta, i)i]di\}}{\partial \theta} = \frac{\partial\{\int \sum_{k=0}^{m} [L_k(i)\cos(kN_r\theta)i]di\}}{\partial \theta} \\ &= -\sum_{k=0}^{m} \{kN_r \sin(kN_r\theta)\int [L_k(i)i]di\} \end{aligned}. \tag{22.84}$$

22.5.3 PARAMETER IDENTIFICATION FROM STANDSTILL TEST DATA

22.5.3.1 Standstill test configuration

The basic idea of standstill test is to apply a short voltage pulse to the phase winding with the rotor blocked, record the current generated in the winding, and then use maximum likelihood estimation to estimate the resistances and inductances of the winding. By performing this test at different current level, the relationship between inductance and current can be curve-fitted with polynomials.

The experimental setup is shown in Figure 22.35. An 8/6 SRM is used in this test. Before testing, the motor is rotated to a specific position (with one of the phase windings aligned, unaligned, or at other positions) and blocked. A DSP system (dSPACE DS1103 controller board) is used to generate the gating signal to a power converter to apply appropriate voltage pulses to that winding. The voltage and current at the winding is sampled and recorded. Later on, the test data is used to identify the winding parameters.

When all the test data are collected, MLE is used to identify the winding parameters (*R* and *L*). The results of identification are validated with the test data: the voltages measured at

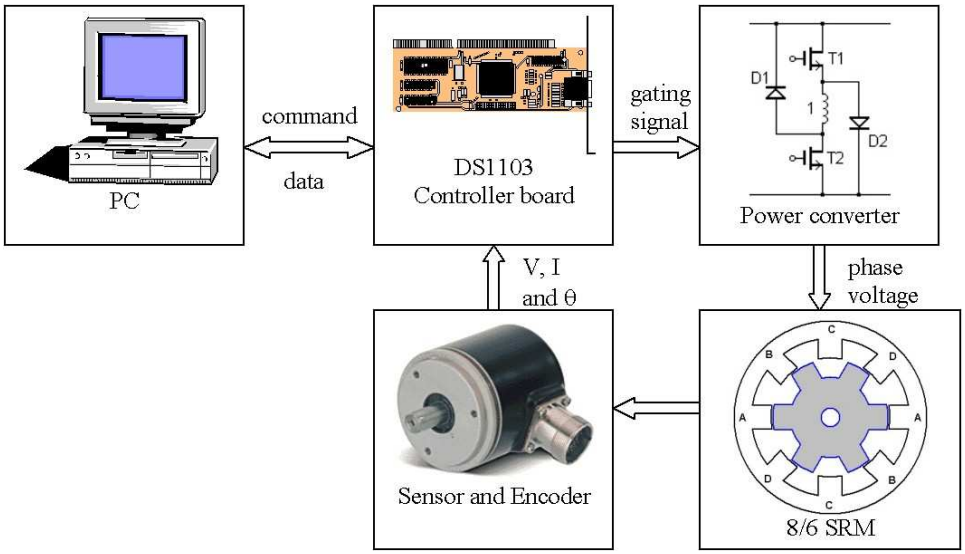

Figure 22.35 Experimental setup

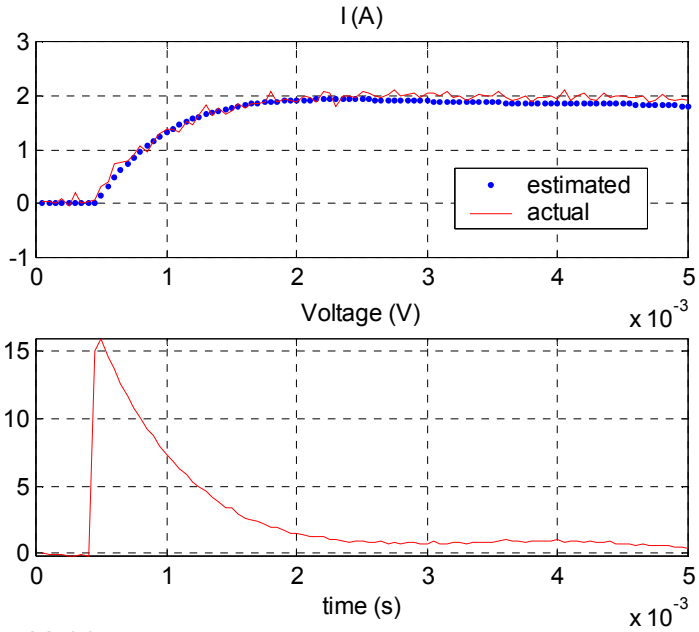

Figure 22.36 Validation of model for standstill test

standstill test are applied to the SRM model and the current responses are compared with the measured currents. From Figure 22.36, the estimated current (dotted curve) matches the measured current (solid curve) very well. This proves that the estimated parameters are quite satisfactory.

22.5.3.2 Standstill test results

The motor used in this test is an 8/6 SRM. Tests are performed at several specific positions for current between 0~50 ampere. The inductance estimation and curve-fitting results at aligned, midway, and unaligned position are shown in Figure 22.37-22.39 (Results are obtained using Matlab/Simulink®).

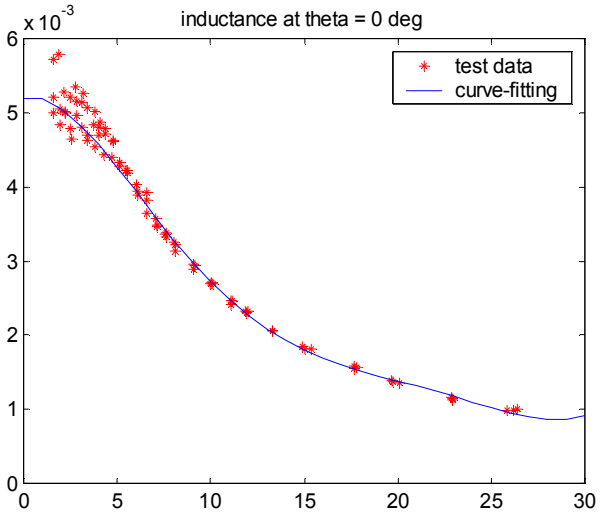

Figure 22.37 Standstill test results for inductance at 0^o

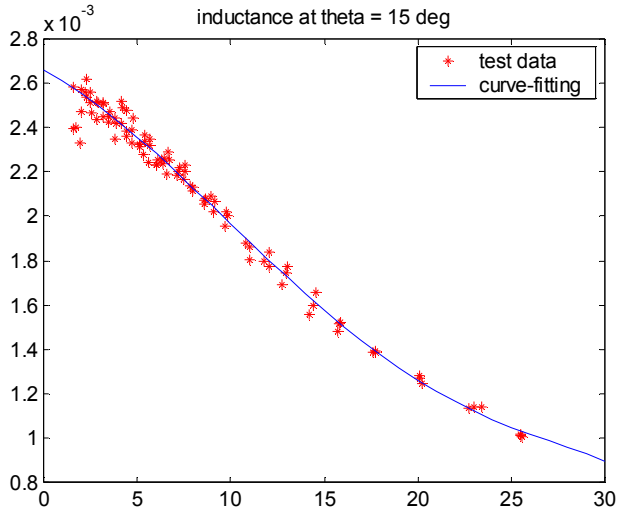

Figure 22.38 Standstill test results for inductance at 15^o

The results show that the inductance at unaligned position doesn't change much with the phase current and can be treated as a constant. The inductances at midway and aligned position decrease when current increases due to saturation.

A 3-D plot of inductance shown in Figure 22.40 depicts the profile of inductance versus rotor position and phase current.

At theta = 0 and 60 degrees, phase A is at its aligned positions and has the highest value of inductance. It decreases when the phase current increases. At theta = 30 degrees, phase A is at its unaligned position and has lowest value of inductance. The inductance here keeps nearly constant when the phase current changes.

In Figure 22.41, the flux linkage versus rotor position and phase current based on the estimated inductance model is shown. The saturation of phase winding at high currents is clearly represented. At aligned position, the winding is highly saturated at rated current.

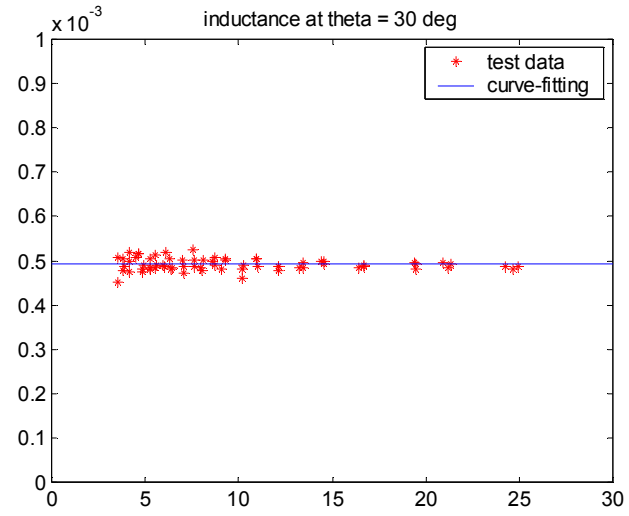

Figure 22.39 Standstill test results for inductance at 30 ^{o}

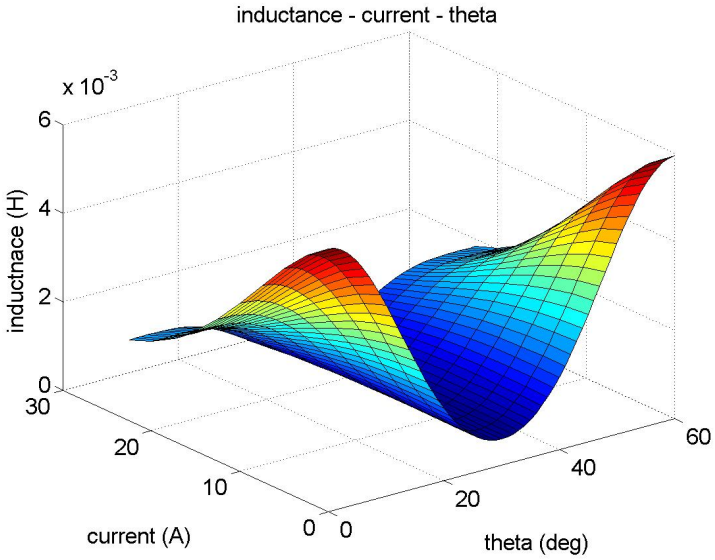

Figure 22.40 Standstill test result: nonlinear phase inductance

22.5.4 Inductance Model of SRM for Online Operation

For online operation case, especially under high load, the losses become significant. There are no windings on the rotor of SRMs. But similar as synchronous machines, there will be circulating currents flowing in the rotor body and makes it works as a damper winding. Considering this, the model structure may be modified as shown in Figure 22.42, with R_d and L_d added to represent the losses on the rotor.

The phase voltage equations can be written as:

$$\begin{bmatrix} L & -L_d \\ 0 & L_d \end{bmatrix} \cdot \begin{bmatrix} \dot{i}_1 \\ \dot{i}_2 \end{bmatrix} = \begin{bmatrix} 0 & R_d \\ -R & -R-R_d \end{bmatrix} \cdot \begin{bmatrix} i_1 \\ i_2 \end{bmatrix} + \begin{bmatrix} 0 \\ 1 \end{bmatrix} V \,, \tag{22.85}$$

where i1 and i2 are the magnetizing current and damper current.

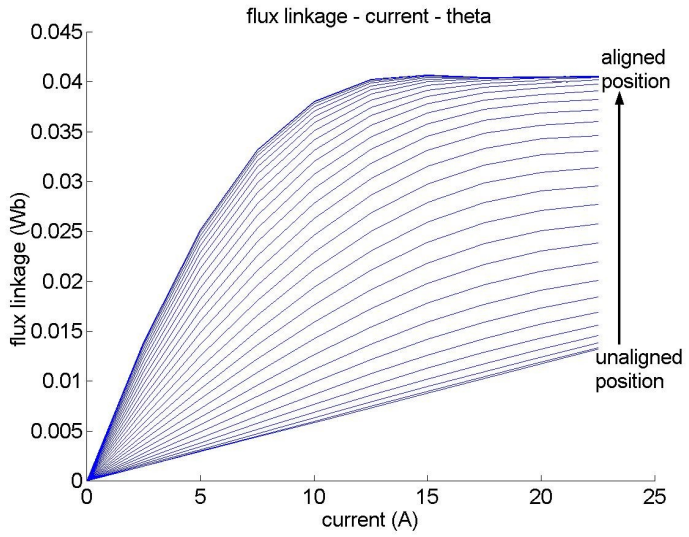

Figure 22.41 Flux linkage at different currents and different rotor positions

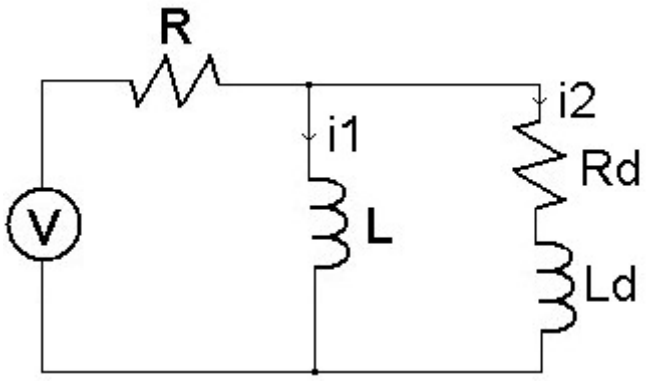

Figure 22.42 Model structure of SRM under saturation

It can be re-written in state space form as:

$$\begin{aligned} \dot{X} &= AX + BU \\ Y &= CX + DU \end{aligned} \tag{22.86}$$

where

$$X = [i_1 \quad i_2],\ U = [V],$$

$$A = \begin{bmatrix} L & -L_d \\ 0 & L_d \end{bmatrix}^{-1} \cdot \begin{bmatrix} 0 & R_d \\ -R & -R-R_d \end{bmatrix},$$

$$B = \begin{bmatrix} L & -L_d \\ 0 & L_d \end{bmatrix}^{-1} \cdot \begin{bmatrix} 0 \\ 1 \end{bmatrix},$$

$$Y = i_1 + i_2 ,$$

$$C = [1 \quad 1] , \text{ and } D = 0 .$$

The torque can be computed as follows (notice that L is the magnetizing winding):

$$\begin{aligned} T &= \frac{\partial W_c(\theta, i_1)}{\partial \theta} = \frac{\partial \{\int [L(\theta, i_1) i_1] di_1\}}{\partial \theta} \\ &= \frac{\partial \{\int \sum_{k=0}^{m} [L_k(i_1) \cos(kN_r \theta) i_1] di_1\}}{\partial \theta} \\ &= -\sum_{k=1}^{m} \{kN_r \sin(kN_r \theta) \int [L_k(i_1) i_1] di_1\} \end{aligned} \tag{22.87}$$

During operation, we can easily measure phase voltage V and phase current $i = i_1 + i_2$. But we cannot measure the magnetizing current (i1) and the damper winding current (i2). Let's assume that the phase parameters R and L obtained from standstill test data are accurate enough for low current case. And we want to attribute all the errors at high current case to damper parameters. If we can estimate the exciting i1 during online operation, then it will be very easy to estimate the damper parameters. This is described in later sections.

22.5.5 TWO-LAYER RECURRENT NEURAL NETWORK FOR DAMPER CURRENT ESTIMATION

22.5.5.1 Structure of Two-layer Recurrent Neural Network

During online operation, there will be motional back EMF in the phase winding. So the exciting current i_1 will be affected by:

Phase voltage V,
Phase current i,
Rotor position θ, and
Rotor speed ω.

To map the relation ship between i_1 and V, i, θ, ω, the neural network structure shown in Figure 22.43 is used. It is a two-layer recurrent neural network.

The first layer is the input layer. The inputs of the network are V, i, θ, ω (with possible delays). One of the outputs, the current i, is also fed back to the input layer to form a recurrent neural network.

The second layer is the output layer. The outputs are i (used as training objective) and i_1.

A hyperbolic tangent sigmoid transfer function – "*tansig*()" is chosen to be the activation function of the input layer, which gives the following relationship between its inputs and outputs:

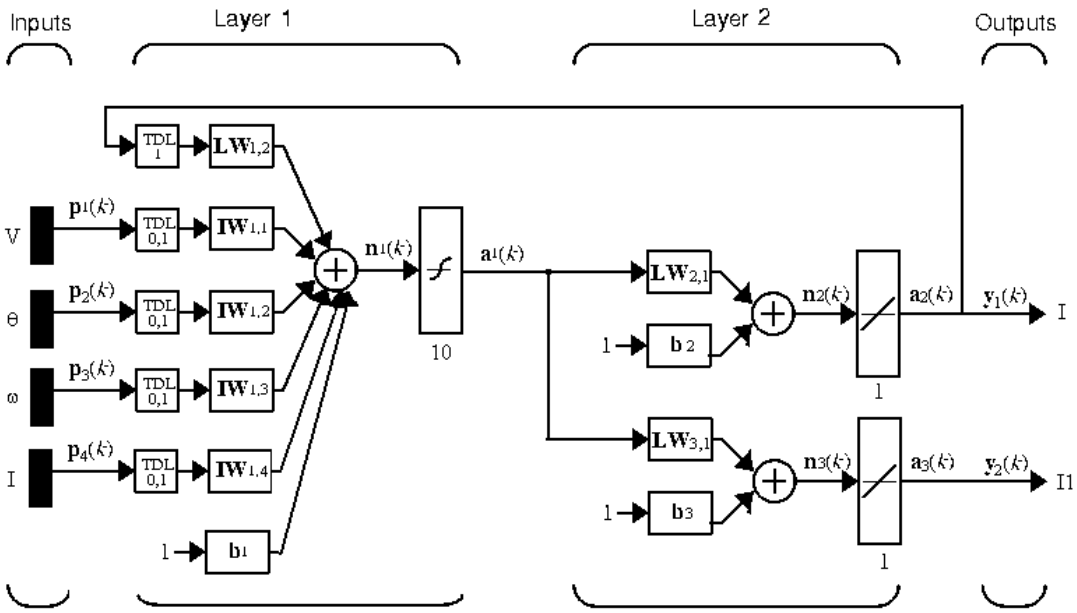

Figure 22.43 Recurrent neural network structure for estimation of exciting current

$$n_1 = \sum_{i=1}^{4} IW_{1,i} \cdot p_i + LW_{1,2} \cdot y_1 + b_1$$

$$a_1 = tansig(n_1) = \frac{2}{1+e^{-2n_1}} - 1 \tag{22.88}$$

A pure linear function is chosen to be the activation of the output layers, which gives:

$$n_2 = LW_{2,1} \cdot a_1 + b_2$$
$$y_1 = a_2 = purelin(n_2) = n_2 \tag{22.89}$$

$$n_3 = LW_{3,1} \cdot a_1 + b_3$$
$$y_2 = a_3 = purelin(n_3) = n_3 \tag{22.90}$$

After the neural network is trained with simulation data (using parameters obtained from standstill test). It can be used to estimate exciting current during on-line operation. When i1 is estimated, the damper current can be computed as

$$i_2 = i - i_1, \tag{22.91}$$

and the damper voltage can be computed as

$$V_2 = V - i \cdot R, \tag{22.92}$$

then the damper resistance Rd and inductance Ld can be identified using output error or maximum likelihood estimation.

22.5.5.2 Training of Neural Network

The data used for training is generated from simulation of SRM model obtained from standstill test.

First, from standstill test result, we can estimate the winding parameters (R and L) and damper parameters (R_d and L_d). The R_d and L_d got from standstill test data may not be accurate enough for online model, but it can be used as initial values that will be improved later.

Second, build an SRM model with above parameters and simulate the motor with hysteresis current control and speed control. The operating data under different reference currents and different rotor speeds are collected and sent to neural network for training.

Third, when training is done, use the trained ANN model to estimate the magnetizing current (i1) from online operating data. Compute damper voltage and current according to Equations 22.91 and 22.92. Then estimate R_d and L_d from the computed V2 and i2 using output error estimation. This R_d and L_d can be treated as improved values of standstill test results.

Repeat above procedures until R_d and L_d are accurate enough to represent online operation (it means that the simulation data matches the measurements well).

In our research, the neural network can map the exciting current from and V, i, θ, ω very well after training of 200 epochs.

22.5.6 Estimation Results and Model Validation

The parameters for damper winding are successfully estimated from operating data by using the neural network mapping described above.

To test the validity of the parameters obtained from above test, a simple on-line test has been performed. In this test, the motor is accelerated with a fixed reference current of 20 ampere. All the operating data such as phase voltages, currents, rotor position, and rotor speed are measured. Then the phase voltages are fed to an SRM model running in Simulink, which has the same rotor position and speed as the real motor. All the phase currents are estimated from the Simulink mode and compared with the measured currents. In Figure 22.44, the phase current responses are shown. The dashed curve is the voltage applied to phase winding; the solid curve is the measured current; and the dotted curve is the estimated current. An enlarged view of the curves for phase A is shown in Figure 22.45. It is clear that the estimation approximates to the measurement quite well.

To compare online model with standstill one, we compute the covariance of the errors between the estimated phase currents and the measured currents. The average covariance for standstill model is 0.9127, while that for online model is 0.6885. It means that the online model gives much better estimation of operating phase currents.

22.5.7 Conclusions

During online operation, the exciting current i1 changes with phase voltage V, rotor position θ, and rotor speed ω. The relationship between them is highly nonlinear and cannot be easily expressed by any analytical equation. The neural network can provide very good mapping if trained correctly. This makes it a good choice for such a task.

Once the NN is trained, it can estimate the exciting current from inputs very quickly, without solving any differential equations that is necessary in conventional methods. So it can

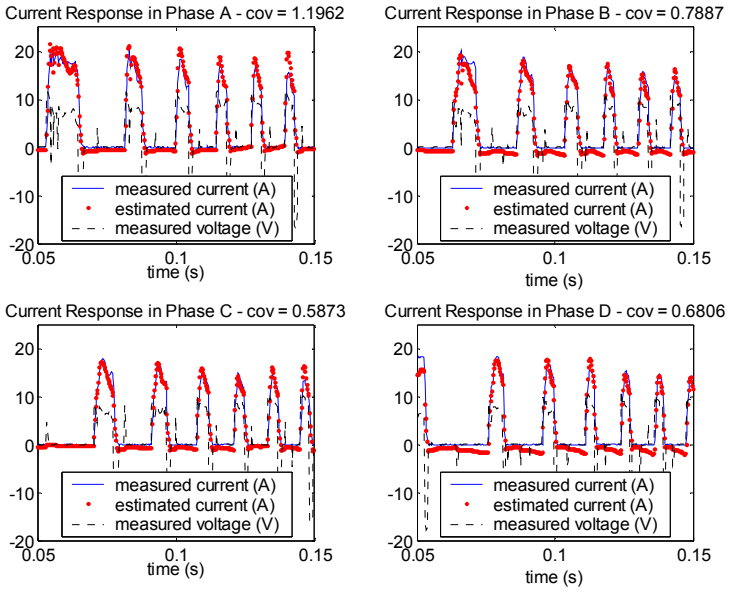

Figure 22.44 Validation of model with on-line operating data

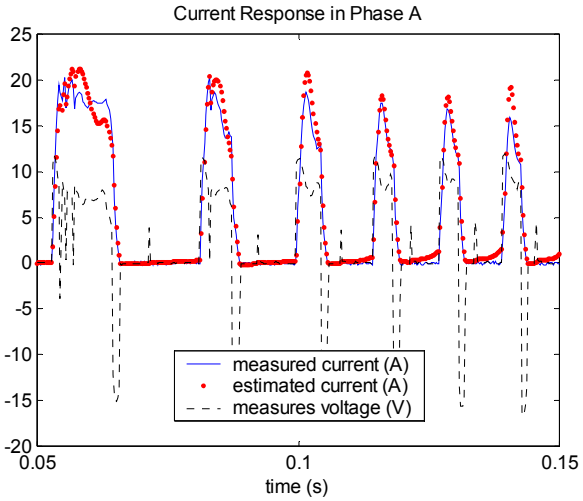

Figure 22.45 Validation of model with on-line operating data (Phase A)

be used for online parameter identification with no computational difficulties. This method has been successfully applied to synchronous machines and induction machines [62,64,65]; it can be applied to SRMs as well.

This section presents the idea and procedure to use artificial neural network to help identify the resistance and nonlinear inductance of SRM winding from operating data. First the resistance and inductance of the magnetizing winding are identified from standstill test data. Then a 2-layer recurrent neural network is setup and trained with simulation data based on standstill model. By applying this neural network to online operating data, the magnetizing current can be estimated and the damper current can be computed. Then the parameters of the damper winding can be identified using maximum likelihood estimation. Tests performed on a 50-ampere 8/6 SRM show satisfactory results of this method.

REFERENCES

1. A Keyhani, S Hao, G Dayal, Maximum likelihood estimation of solid-rotor synchronous machine parameters from SSFR test data, IEEE/PES 1989 Winter Meeting, New York.
2. YN Yu, HAM Moussa, Experimental determination of exact equivalent circuit parameters of synchronous machines, IEEE Transactions on Power App. Systems, Vol. PAS-90, No. 6, November/December 1971, Pages 2555-2560.
3. MVK Chari, SH Minnich, RP Schulz, Improvement in accuracy of prediction of electrical machine constants, and generator models for subsynchronous resonance conditions, EPRI Project RP-1288 and RP-1513, Report #EL-3359, Vol. 1, 2 and 3, 1984, 1987.
4. SH Minnich, RP Schulz, DH Baker, RG Farmer, DK Sharma, JH Fish, Saturation functions for synchronous generators from finite elements, IEEE Transactions on Energy Conversion, Vol. EC-2, No. 4, December 1987, Pages 680-692.
5. JJ Sanchez-Gasca, CJ Bridenbaugh, CEJ Bowler, JS Edmonds, Trajectory sensitivity based identification of synchronous generator and excitation system parameters, IEEE/PES Winter Meeting, New York, 1988.
6. ES Bose, KC Balda, RG Harley, RC Beck, Time-domain identification of synchronous machine parameters from simple standstill tests, IEEE/PES Winter Meeting, New York, 1988.
7. JC Balda, MF Hadingham, RE Fairbairnm RC Harley, E Eitelberg, Measurement of frequency response method – Part I: Theory, IEEE Transactions on Energy Conversion, Vol. EC-2, No. 4, December 1987, Pages 646-651.
8. JC Balda, MF Hadingham, RE Fairbairnm RC Harley, E Eitelberg, Measurement of frequency response method – Part II: Measured results, IEEE Transactions on Energy Conversion, Vol. EC-2, No. 4, December 1987, Pages 652-657.
9. FP deMello, LN Hannett, Determination of synchronous machine electrical characteristics by test, IEEE Transaction on Power App. Systems, Vol. PAS-102, December 1983, Pages 3810-3815.
10. IEEE Committee report, Current usage and suggested practices in power system stability simulations for synchronous machines, IEEE Transactions on Energy Conversion, Vol. EC-1, No. 1, March 1986, Pages 77-93.
11. PL Dandeno, AT Poray, Development of detailed turbogenerator equivalent circuits from standstill frequency response measurements, IEEE Transactions on Power App. Systems, Vol. PAS-100, No. 4, April 1981, Pages 1646-1655.
12. PL Dandeno, P Kundur, AT Poray, M Coultes, Validation of turbogenerator stability models by comparison with power system tests, IEEE Transactions on Power App. Systems, Vol. PAS-100, April 1981, Pages1637-1645.
13. ME Coultes, W Watson, Synchronous machine models by standstill frequency response tests, IEEE Transactions on Power App. Systems, Vol. PAS-100, No. 4, 1981, Pages 1480-1489.
14. IEEE standard procedure for obtaining synchronous machine parameters by standstill frequency response testing, IEEE Standards, 115A-1987.
15. SD Umans, JA Mallick, GL Wilson, Modeling of solid rotor turbogenerators – Part I: Theory and techniques, IEEE Transactions on Power App. Systems, Vol. PAS-97, No. 1, 1978, Pages 269-277.
16. SD Umans, JA Mallick, GL Wilson, Modeling of solid rotor turbogenerators – Part II: Example of modellderivation and use in digital simulation, IEEE Transactions on Power App. Systems, Vol. PAS-97, No. 1, 1978, Pages 278-291.
17. SD Umans, Modeling of solid rotor turbogenerators, Ph.D. Thesis, Massachusetts Institute of Technology, January, 1976.
18. IM Canay, Extended Synchronous Machine Model for the Calculation of Transient Processes and Stability, Electric Machine and Electromechanics: An International Quarterly, 1977, Pages 137-150.

19. A Keyhani, SM Miri, Observers for tracking of synchronous machine parameters and detection of incipient faults, IEEE Transactions on Energy Conversion, Vol. EC-1, No. 2, June 1986, Pages 184-192.
20. D Marquardt, An algorithm for least-square estimation if nonlinear parameters, Journal of Soc. Indust. And Appl. Math. II, 1963, Pages 431-441
21. "MACSYMA, Comuter-Aided Mathematics Group of Symbolics, Symbolics Inc., Eleven Cambridge Center, Cambridge, Massachusetts 02142.
22. A Keyhani, S Hao, G Dayal, The effect of noise on frequency-domain parameter estimation of synchronous machine models, IEEE/PES 1989 Winter Meeting, New York.
23. LX Le, WJ Wilson, Synchronous Machine Parameter Identification: A Time Domain Approach, IEEE Transactions on Energy Conversion, Vol. 3, No. 2, June 1988, Pages 241-247.
24. N Jaleeli, MS Bourawi, JH Fish III, A quasilinearization based algorithm for identification of transient and subtransient parameters of synchronous machines, IEEE Transactions on Power Systems, Vol. PWRS-1, No. 3, August 1986, Pages 46-52.
25. M Namba, T Nishiwaki, S Yokokawa, K Ohtsuka, Y Ueki, Identification of parameters for power system stability analysis using Kalman filter, IEEE Transactions on App. Systems, Vol. PAS-100, July 1981, Pages 3304-3311.
26. KJ Astrom, Maximum likelihood and prediction error methods, Automatica, Vol. 16, 1980, Pages 551-574.
27. NK Gupta, RK Mehra, Computational aspects of maximum likelihood estimation and reduction in sensitivity function calculations, IEEE Transactions on Automatic Control, VOL. AC-19, No. 6, December 1974, Pages 774-783.
28. GC Goodwin, RL Payne, Dynamic System Identification, Academic Press, New York, 1977
29. KJ Astrom and T Soderstrom, Uniqueness of the maximum likelihood estimates of the parameters of an ARMA model, IEEE Transactions on Automatic Control, Vol. 19, 1974, Pages 769-773.
30. T Bohlin, On the maximum likelihood method of idetification, IBM Journal on Research and Development, Vol. 4, No. 1, 1970, Pages 41-51.
31. JE Dennis, RB Schnabel, Numerical Methods for Unconstrained Optimization and Nonlinear Equations, Prentice-Hall, Inc., Englewood Cliffs, New Jersey, 1983.
32. RP Schulz, Synchronous Machine Modeling, IEEE 1975 Symposium, "Adequacy and Philosophy of Modeling: Dynamic System Performance," IEEE Monograph 75 CH0970-4 PWR, Pages 24-28.
33. WB Jackson, EL Winchester, Direct- and Quadrature-Axis Equivalent Circuits for Solid-Rotor Turbine Generators, IEEE Transactions on Power App. Systems, Vol. PAS-88, No. 7, July 1969, Pages 1121-1136.
34. GR Slemon, Modeling of induction machines for electric drives, IEEE Transaction on Industry Applications, Vol. 25, No. 6, 1989 p. 1126-1131
35. NR Klaes, Parameter identification of an induction machine with regard to dependencies on saturation, IEEE Transaction on Industry Applications, Vol. 29, No. 6, 1993 p. 1135-1140
36. SI Moon, A Keyhani, S Pillutla, Nonlinear neural-network modeling of an induction machine, IEEE Transaction on Control Systems Technology, Vol. 7, No. 2, 1999, p. 203-211
37. JA de Kock, FS van der Merwe, HJ Vermeulen, Induction motor parameter estimation through an output error technique, IEEE Transaction on Energy Conversion, Vol. 9, No. 1, 1994, p. 69-76
38. AMN Lima, CB Jacobina, EBF. de Souza, Nonlinear parameter estimation of steady-state induction machine models, IEEE Transaction on Industrial Electronics, Vol. 44, No. 3, 1997, p. 390-397
39. LA de Souza Ribeiro, CB Jacobina, AM Nogueira Lima, Linear parameter estimation for induction machines considering the operating conditions , IEEE Transaction on Power Electronics, Vol. 14, No. 1, 1999, p. 62-73

40. P Pillay, R Nolan, T Haque, Application of genetic algorithms to motor parameter determination for transient torque calculations, IEEE Transaction on Industry Applications, Vol. 33, No. 5, 1997 p. 1273-1282
41. E Mendes, A Razek, A simple model for core losses and magnetic saturation in induction machines adapted for direct stator flux orientation control, IEE Conference Publication, v. 399, 1994, p.192-197
42. S Ansuj, F Shokooh, R Schinzinger, Parameter estimation for induction machines based on sensitivity analysis, IEEE Transaction on Industry Applications, Vol. 25, No. 6, 1989, p. 1035-1040
43. J Stephan, M Bodson, J Chiasson, Real-time estimation of the parameters and fluxes of induction motors, IEEE Transaction on Industry Applications, Vol. 30, No. 3, 1994, p. 746-759
44. X Xu, DW Novotny, Implementation of direct stator flux orientation control on a versatile DSP based system, IEEE Transaction on Industry Applications, Vol. 27, No. 4, 1991, p. 694-700
45. JK Seok, SI Moon, SK Sul, Induction machine parameter identification using PWM inverter at standstill, IEEE Transaction on Energy Conversion, Vol. 12, No. 2, 1997, p. 127-132
46. C Wang, DW Novotny, TA Lipo, An automated rotor time constant measurement system for indirect field-oriented drives, IEEE Transaction on Industry Applications, Vol. 24, No. 1, 1988, p. 151-159
47. YN Lin, CL Chen, Automatic IM parameter measurement under sensorless field-oriented control, IEEE Transaction on Industrial Electronics, Vol. 46, No. 1, 1999, p. 111-118
48. SK Sul, A novel technique of rotor resistance estimation considering variation of mutual inductance, IEEE Transaction on Industry Applications, Vol. 25, No. 4, 1989, p. 578-587
49. T Noguchi, S Kondo, I Takahashi, Field-oriented control of an induction motor with robust on-line tuning of its parameters, IEEE Transaction on Industry Applications, Vol. 33 No. 1, 1997, p 35-42.
50. LC Zai, CL DeMarco, TA Lipo, An extended Kalman filter approach to rotor time constant measurement in PWM induction motor drives, IEEE Transaction on Industry Applications, Vol. 28, No. 1, 1992, p. 96-104
51. DJ Atkinson, PP Acarnley, JW Finch, Observers for induction motor state and parameter estimation, IEEE Transaction on Industry Applications, Vol. 27, No. 6, 1991, p. 1119-1127
52. S Wade, MW Dunnigan, BW Williams, New method of rotor resistance estimation for vector-controlled induction machines, IEEE Transaction on Industrial Electronics, Vol. 44, No. 2, 1997, p. 247-257
53. K Matsuse, T Yoshizumi, S Katsuta, S Taniguchi, High response flux control of direct-field-oriented induction motor with high efficiency taking core loss into account, IEEE Transaction on Industry Applications, Vol.35, No.1, 1999, p.62-69
54. B Robyns, PA Sente, HA Buyse, F Labrique, Influence of digital current control strategy on the sensitivity to electrical parameter uncertainties of induction motor indirect field-oriented control, IEEE Transaction on Power Electronics, Vol.14, No.4, 1999, p.690-699
55. K Akatsu, A Kawamura, Online rotor resistance estimation using the transient state under the speed sensorless control of induction motor, IEEE Transaction on Power Electronics, Vol. 15, No. 3, 2000, pp. 553-560
56. SJ Chapman, Electric Machinery Fundamentals, 2nd Edition, New York: McGraw-Hill, 1991
57. V Utkin, J Guldner, J. Shi, Sliding mode control in electromechanical systems, Taylor & Francis, 1999
58. S Mir, I Husain, ME Elbuluk, Switched Reluctance Motor Modeling with On-line Parameter Identification. IEEE Transactions on Industry Applications, Vol. 34, No. 4, July/August 1998.
59. B Fahimi, G Suresh, J Mahdavi, M. Ehsani, A New Approach to Model Switched Reluctance Motor Drive Application to Dynamic Performance Prediction, Control and Design. Power Electronics Specialists Conference, Vol. 2, 1998.

60. L Xu and E Ruckstadter, Direct Modeling of Switched Reluctance Machine by Coupled Field-Circuit Method. IEEE Transactions on Energy Conversion, Vol. 10, Issue 3, September 1995.
61. SI Moon, A Keyhani. Estimation of Induction Machine Parameters from Standstill Time-Domain Data. IEEE Transactions on Industry Applications, Vol. 30, No. 6, November/December 1994.
62. A Keyhani, H Tsai, T Leksan. Maximum Likelihood Estimation of Synchronous Machine Parameters from Standstill Time Response Data. 1993 IEEE/PES Winter Meeting, Columbus, OH. Jan. 31- Feb. 5, 1993.
63. KM Passino. Intelligent Control: Biomimicry for Optimization, Adaptation, and Decision-Making in Computer Control and Automation. Textbook, The Ohio State University, March 2001.
64. S Pillutla, A Keyhani. Neural Network Based Modeling of Round Rotor Synchronous Generator Rotor Body Parameters from Operating Data. IEEE Transactions on Energy Conversion, 1998.
65. S Pillutla, A Keyhani. Neural Network Based Saturation Model of Round Rotor Synchronous Generator Rotor. IEEE Transactions on Energy Conversion, 1998.
66. SS Ramamurthy, RM Schupbach, JC Balda. Artificial Neural Networks based Models for the Multiply Excited Switched Reluctance Motor. APEC 2001.
67. B Fahimi, G Suresh, J Mahdavi, M Ehsani. A New Approach to Model Switched Reluctance Motor Drive Application to Dynamic Performance Prediction, Control and Design. Power Electronics Specialists Conference, Vol. 2, 1998.
68. W Lu, A Keyhani, A Fardoun, Neural network-based modeling and parameter identification of switched reluctance motors, IEEE Transactions on Energy Conversion, Vol.18 Issue 2, June 2003, Pages 284 -290
69. HB Karayaka, A Keyhani, GT Heydt, BL Agrawal, DA Selin, Synchronous generator model identification and parameter estimation from operating data, IEEE Transactions on Energy Conversion, Vol.18 Issue 1, March 2003, Pages 121 –126
70. W Lu, A Keyhani, H Klode, AB Proca, Modeling and parameter identification of switched reluctance motors from operating data using neural networks, IEEE International Electric Machines and Drives Conference, 2003 (IEMDC'03), Vol. 3, 1-4 June, 2003, Pages 1709 -1713
71. AB Proco, A Keyhani, Induction motor parameter identification from operating data for electric drive applications**,** 1999. Proceedings of 18th Digital Avionics Systems Conference, Volume 2, 24-29 Oct. 1999, Pages: 8.C.2-1 -8.C.2-6
72. AB Proca, A Keyhani, Identification of variable frequency induction motor models from operating data**,** IEEE Transactions on Energy Conversion, Volume 17, Issue 1, March 2002, Pages: 24 –31
73. A El-Serafi, A Abdallah, M El-Sherbiny, E Badawy, Experimental Study of the Saturation and the Cross-Magnetizing Phenomenon in Saturated Synchronous Machines, IEEE Transactions on Energy Conversion, Vol. EC-3, Dec. 1988, pp. 815-823.
74. F De Mello, L Hannett, Representation of Saturation in Synchronous Machines, IEEE Transactions on Power Systems, v. 1, Nov. 1986, pp. 8-14.
75. S Minnich, R Schulz, D Baker, D Sharma, R Farmer, J Fish, Saturation functions for synchronous generators from finite elements, IEEE Transactions on Energy Conversion, v. 2, Dec. 1987, pp. 680-687.
76. H Tsai, A Keyhani, JA Demcko, and DA Selin, Development of a Neural Network Saturation Model for Synchronous Generator Analysis, IEEE Transactions on Energy Conversion, v. 10, no. 4, Dec 1995. pp. 617-624.
77. L Xu, Z Zhao, and J Jiang, On-line Estimation of Variable Parameters of Synchronous Machines Using a Novel Adaptive Algorithm – Estimation and Experimental Verification, IEEE Transactions on Energy Conversion, Sept. 1997. v. 12, no. 3, pp. 200-210.
78. H Tsai, A Keyhani, JA Demcko, RG Farmer, On-line synchronous machine parameter estimation from small disturbance operating data, IEEE Transactions on Energy Conversion, v. 10, no. 1, Mar. 1995, pp. 25-36.

79. KS Narendra and K Parthasarathy, Identification and control of dynamical systems using neural networks, IEEE Transactions on Neural Networks, v. 1, pp. 4-27, 1990.
80. IM Canay, Causes of Discrepancies on Calculation of Rotor Quantities and Exact Equivalent Diagrams of the Synchronous Machine, IEEE Transactions on Power Apparatus and Systems, v. PAS-88, no. 7, July 1969. pp. 1114-1120.
81. JL Kirtley Jr, On Turbine-Generator Rotor Equivalent Circuit Structures for Empirical Modeling of Turbine Generators, IEEE Transactions on Power Systems, v. PWRS-9(1), 1994, pp. 269-271.
82. I Kamwa, P Viarouge, J Dickinson, Identification of Generalized Models of Synchronous Machines from Time-Domain Tests, IEE Proceedings C, 138 (6), Nov. 1991. pp. 485-498.
83. S Salon, Obtaining Synchronous Machine Parameters from Test, Symposium on Synchronous Machine Modeling for Power Systems Studies. Paper No. 83THO101-6-PWR. Available from IEEE Service Center, Piscataway, NJ, USA.
84. SR Chaudhary, S Ahmed-Zaid, NA Demerdash, An artificial neural network model for the identification of saturated turbo-generator parameters based on a coupled finite-element/state-space computational algorithm, IEEE Transactions on Energy Conversion, v. 10, Dec. 1995, pp. 625-633.
85. JA Demcko, JP Chrysty, Self-Calibrating Power Angle Instrument, EPRI GS-6475, v. 2, Research Project 2591-1 Final Report, EPRI, August 1989.
86. MA Arjona, DC Macdonald, A new lumped steady-state synchronous machine model derived from finite element analysis, IEEE Transactions on Energy Conversion v. 14, no. 1 March 1999. pp. 1-7.
87. H Karayaka, A Keyhani, B Agrawal, D Selin, G Heydt, Identification of Armature, Field and Saturated Parameters of a Large Steam Turbine-Generator from Operating Data, to appear in IEEE Transactions on Energy Conversion, Preprint Order No. PE064EC (05-1999).
88. M Hagan, MB Menhaj, Training Feedforward Networks with the Marquardt Algorithm, IEEE Transactions on Neural Networks, v. 5, no. 6, pp. 989-993, November 1994.
89. H Karayaka, A Keyhani, B Agrawal, D Selin, G Heydt, Methodology Development for Estimation of Armature Circuit and Field Winding Parameters of Large Utility Generators, IEEE Transactions on Energy Conversion, v.14, no. 4, Dec. 1999, pp. 901-908.
90. A Derdiyok, H Rehman, MK Guven, N Inanc, and L Xu, A robust sliding mode observer for speed estimation of induction machine, APEC 2001, vol. 1, p.413-418

APPENDIX A

The complex nonlinear equations which relate the d-axis SSFR3 model parameters with the time constants of the corresponding transfer function can be concisely written as:

$$f_i(\bar{x}) = \bar{y}_i + g_i(\bar{x}, \bar{y}) + \zeta_i = 0$$

where $i = 1, \ldots, 10$.

Vector $\bar{x}$ and $\bar{y}$ are defined in Table 22.1. ζ_i represents the noise associated with each element y_i. This is because noise is inherently present in the test data.

The above set of nonlinear equations can be expanded as:

$$f_1(\bar{x}) = y_1 - y_0 + x_1 + \zeta_1 = 0 \tag{A.1}$$

$$\begin{aligned} f_2(\bar{x}) = y_2 - [&(x_9 + x_5 + x_2 + x_1)x_4x_7y_0 \\ &+ (x_2 + x_1)x_9x_7 + (x_2 + x_1)x_5x_7y_0 \\ &+ (x_5 + x_2 + x_1)x_9x_4y_0 \\ &+ (x_2 + x_1)x_5x_9y_0 + (x_9 + x_5 + x_2)x_1x_4x_7 \\ &+ (x_2x_9 + x_2x_5)x_1x_7 + (x_5 + x_2)x_1x_9x_4 \\ &+ x_1x_2x_5x_9]/[(y_0 + x_1)x_3x_6x_8] \\ &+ \zeta_2 = 0 \end{aligned} \tag{A.2}$$

$$\begin{aligned} f_3(\bar{x}) = y_3 - [&x_6(x_9 + x_5 + x_2 + x_1)x_4y_0 \\ &+ x_6(x_2 + x_1)x_9y_0 + x_6(x_2 + x_1)x_5y_0 \\ &+ x_6(x_9 + x_5 + x_2)x_1x_4 + x_6x_2x_9x_1 \\ &+ x_6x_2x_1x_5 + x_3(x_9 + x_5 + x_2 + x_1)x_7y_0 \\ &+ x_3(x_5 + x_2 + x_1)x_9y_0 \\ &+ x_3(x_9 + x_5 + x_2)x_1x_7 + x_3(x_5 + x_2)x_1x_9 \\ &+ x_8(x_4 + x_2 + x_1)x_7y_0 \\ &+ x_8(x_5 + x_2 + x_1)x_4y_0 + x_8(x_2 + x_1)x_5y_0 \\ &+ x_8(x_4 + x_2)x_1x_7 + x_8(x_5 + x_2)x_1x_4 \\ &+ x_8x_1x_2x_5]/[(y_0 + x_1)x_3x_6x_8] \\ &+ \zeta_3 = 0 \end{aligned} \tag{A.3}$$

$$
\begin{aligned}
f_4(\bar{x}) = y_4 - [&x_3x_6(x_9 + x_5 + x_2 + x_1)y_0 \\
&+ x_3x_6x_1x_9 + x_3x_6x_1(x_5 + x_2) \\
&+ x_8x_6(x_4 + x_2 + x_1)y_0 + x_8x_6x_1(x_4 + x_2) \\
&+ x_3x_8(x_7 + x_5 + x_2 + x_1)y_0 \\
&+ x_3x_8x_1(x_7 + x_5 + x_2)]/[(y_0 + x_1)x_3x_6x_8] \\
&+ \zeta_4 = 0
\end{aligned} \tag{A.4}
$$

$$
\begin{aligned}
f_5(\bar{x}) = y_5 - [&x_4x_7(x_9 + x_5 + x_2 + x_1) \\
&+ x_7x_9(x_2 + x_1) + x_7x_5(x_1 + x_2) \\
&+ x_7x_4(x_5 + x_2 + x_1) \\
&+ x_9x_5(x_1 + x_2)]/[x_3x_6x_8] \\
&+ \zeta_5 = 0
\end{aligned} \tag{A.5}
$$

$$
\begin{aligned}
f_6(\bar{x}) = y_6 - [&x_6(x_9 + x_5 + x_2 + x_1)x_4 \\
&+ x_6(x_2 + x_1)x_9 + x_5x_6(x_2 + x_1) \\
&+ x_3(x_9 + x_5 + x_2 + x_1)x_7 \\
&+ x_3x_9(x_5 + x_2 + x_1) \\
&+ x_8(x_4 + x_2 + x_1)x_7 \\
&+ x_8(x_5 + x_2 + x_1)x_4 \\
&+ x_8x_5(x_1 + x_2)]/[x_3x_6x_8] \\
&+ \zeta_6 = 0
\end{aligned} \tag{A.6}
$$

$$
\begin{aligned}
f_7(\bar{x}) = y_7 - [&x_3x_6(x_9 + x_5 + x_2 + x_1) \\
&+ x_8x_6(x_4 + x_2 + x_1) \\
&+ x_3x_8(x_7 + x_5 + x_2 + x_1)]/[x_3x_6x_8] \\
&+ \zeta_7 = 0
\end{aligned} \tag{A.7}
$$

$$
f_8(\bar{x}) = y_8 - x_1 / x_8 + \zeta_8 = 0 \tag{A.8}
$$

$$
f_9(\bar{x}) = y_9 - x_4x_7 /(x_3x_6) + \zeta_9 = 0 \tag{A.9}
$$

$$
f_{10}(\bar{x}) = y_{10} - x_4 / x_3 - x_7 / x_6 + \zeta_{10} = 0 \tag{A.10}
$$

APPENDIX B

The differential equations of the standstill d- and q-axis circuit model (see Figure B1), assuming the field winding is short-circuited, can be written as:

D-axis:

$$v_d = -R_a i_d + p\lambda_d \tag{B.1}$$

$$0 = R_{1d} i_{1d} + p\lambda_{1d} \tag{B.2}$$

$$0 = R_{2d} i_{2d} + p\lambda_{2d} \tag{B.3}$$

$$0 = R_{fd} i_{fd} + p\lambda_{fd} \tag{B.4}$$

where $p : d/dt$

$$\lambda_d = -(L_l + L_{ad}) i_d + L_{ad}(i_{fd} + i_{1d} + i_{2d}) \tag{B.5}$$

$$\lambda_{1d} = (L_{ad} + L_{f12d} + L_{1d}) i_{1d} + L_{ad}(i_{2d} + i_{fd} - i_d) + L_{f12d}(i_{2d} + i_{fd}) \tag{B.6}$$

$$\lambda_{2d} = (L_{ad} + L_{f12d} + L_{f2d} + L_{2d}) i_{2d} + L_{ad}(i_{1d} + i_{fd} - i_d) + L_{f12d}(i_{1d} + i_{fd}) + L_{f2d} i_{fd} \tag{B.7}$$

$$\lambda_{fd} = (L_{ad} + L_{f12d} + L_{f2d} + L_{fd}) i_{fd} + L_{ad}(i_{1d} + i_{2d} - i_d) + L_{f12d}(i_{1d} + i_{2d}) + L_{f2d} i_{2d} \tag{B.8}$$

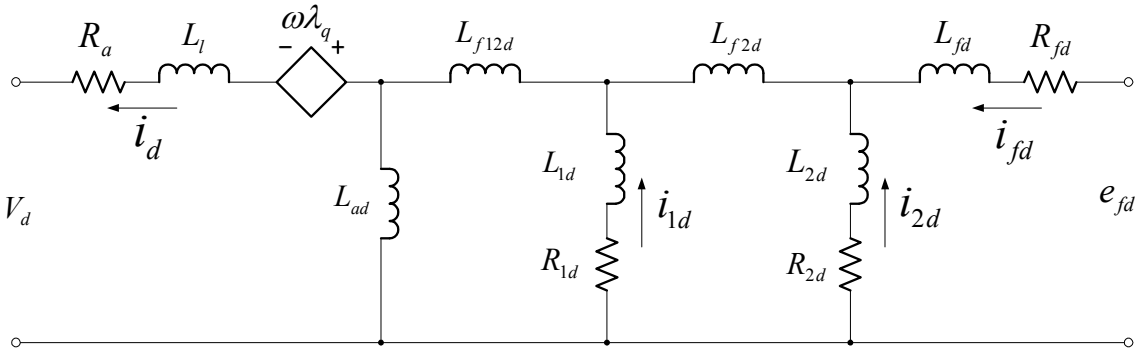

(a) d-axis circuit

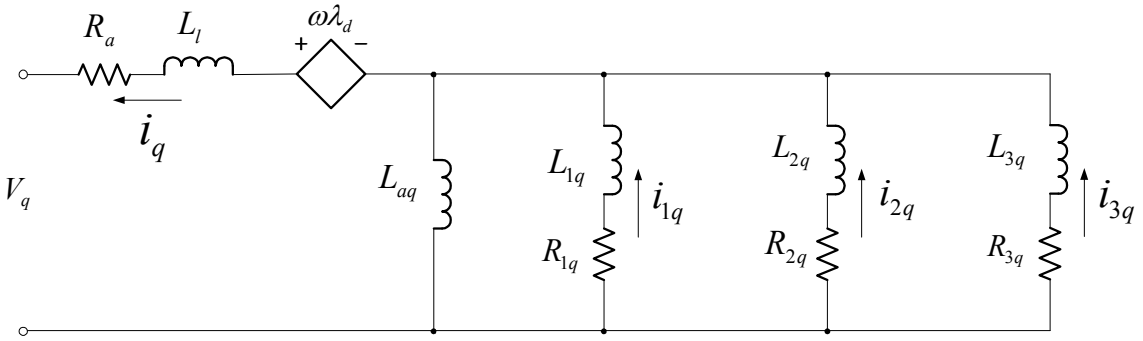

(b) q-axis circuit

Figure 22.B1 SSFR3 Model Structures

Defining:

$$X = \begin{bmatrix} i_d & i_{1d} & i_{2d} & i_{fd} \end{bmatrix}^T$$

$$U = \begin{bmatrix} v_d \end{bmatrix}$$

Equation B.1 to B.8 can be written as the following:

$$F_d(\theta_d)\dot{X} = G_d(\theta_d)X + DU \tag{B.9}$$

where $\dot{X} = dX/dt$

$$D = \begin{bmatrix} 1 & 0 & 0 & 0 \end{bmatrix}^T$$

$$\begin{aligned} \theta_d &= \begin{bmatrix} L_{ad}, L_{f12d}, R_{1d}, L_{1d}, L_{f2d}, R_{2d}, L_{2d}, R_{fd}, L_{fd} \end{bmatrix} \\ &= \begin{bmatrix} \theta_1, \theta_2, \theta_3, \theta_4, \theta_5, \theta_6, \theta_7, \theta_8, \theta_9 \end{bmatrix} \end{aligned}$$

$$F_d(\theta_d) = \begin{bmatrix} -L_l - \theta_1 & \theta_1 & \theta_1 & \theta_1 \\ -\theta_1 & \theta_1 + \theta_2 + \theta_4 & \theta_1 + \theta_2 & \theta_1 + \theta_2 \\ -\theta_1 & \theta_1 + \theta_2 & \theta_1 + \theta_2 + \theta_5 + \theta_7 & \theta_1 + \theta_2 + \theta_5 \\ -\theta_1 & \theta_1 + \theta_2 & \theta_1 + \theta_2 + \theta_5 & \theta_1 + \theta_2 + \theta_5 + \theta_9 \end{bmatrix}$$

$$G_d(\theta_d) = \begin{bmatrix} R_a & 0 & 0 & 0 \\ 0 & -\theta_3 & 0 & 0 \\ 0 & 0 & -\theta_5 & 0 \\ 0 & 0 & 0 & -\theta_8 \end{bmatrix}$$

Now Equation B.9 can be rewritten as:

$$\begin{aligned} \dot{X} &= F_d^{-1}(\theta_d)G_d(\theta_d)X + F_d^{-1}(\theta_d)DU \\ &= \overline{A}_d X + \overline{B}_d U \end{aligned} \tag{B.10}$$

where

$$\begin{aligned} \overline{A}_d &= F_d^{-1}(\theta_d)G_d(\theta_d) \\ \overline{B}_d &= F_d^{-1}(\theta_d)D \end{aligned}$$

The discrete dynamic representation of Equation B.10 is

$$X(k+1) = A_d(\theta_d)X(k) + B_d(\theta_d)U(k) \tag{B.11}$$

The derivation of discrete system matrices, $A_d(\theta_d)$ and $B_d(\theta_d)$, from continuous system matrices, $\overline{A}_d(\theta_d)$ and $\overline{B}_d(\theta_d)$, is given in reference [19].

Q-axis:

$$v_q = -R_a i_q + p\lambda_q \tag{B.12}$$

$$0 = R_{1q} i_{1q} + p\lambda_{1q} \tag{B.13}$$

$$0 = R_{2q} i_{2q} + p\lambda_{2q} \tag{B.14}$$

$$0 = R_{3q} i_{3q} + p\lambda_{3q} \tag{B.15}$$

where $p : d/dt$

$$\lambda_q = -(L_l + L_{aq}) i_q + L_{aq}(i_{1q} + i_{2q} + i_{3q}) \tag{B.16}$$

$$\lambda_{1q} = (L_{1q} + L_{aq}) i_{1q} + L_{aq}(i_{2q} + i_{3q} - i_q) \tag{B.17}$$

$$\lambda_{2q} = (L_{2q} + L_{aq}) i_{2q} + L_{aq}(i_{1q} + i_{3q} - i_q) \tag{B.18}$$

$$\lambda_{3q} = (L_{3q} + L_{aq}) i_{3q} + L_{aq}(i_{1q} + i_{2q} - i_q) \tag{B.19}$$

$$X = \begin{bmatrix} i_q & i_{1q} & i_{2q} & i_{3q} \end{bmatrix}^T$$

$$U = \begin{bmatrix} v_q \end{bmatrix}$$

Equation B.12 to B.19 can be put into the form of

$$F_q(\theta_q)\dot{X} = G_q(\theta_q)X + DU \tag{B.20}$$

where $\dot{X} = dX/dt$

$$\begin{aligned} \theta_q &= \begin{bmatrix} L_{aq}, R_{1q}, L_{1q}, R_{2q}, L_{2q}, R_{3q}, L_{3q} \end{bmatrix} \\ &= \begin{bmatrix} \theta_1, \theta_2, \theta_3, \theta_4, \theta_5, \theta_6, \theta_7 \end{bmatrix} \end{aligned}$$

$$F_q(\theta_q) = \begin{bmatrix} -L_l - \theta_1 & \theta_1 & \theta_1 & \theta_1 \\ -\theta_1 & \theta_1 + \theta_3 & \theta_1 & \theta_1 \\ -\theta_1 & \theta_1 & \theta_1 + \theta_5 & \theta_1 \\ -\theta_1 & \theta_1 & \theta_1 & \theta_1 + \theta_7 \end{bmatrix}$$

$$G_q(\theta_q) = \begin{bmatrix} R_a & 0 & 0 & 0 \\ 0 & -\theta_2 & 0 & 0 \\ 0 & 0 & -\theta_4 & 0 \\ 0 & 0 & 0 & -\theta_6 \end{bmatrix}$$

Now Equation B.20 can be rewritten as:

$$\begin{aligned} \dot{X} &= F_q^{-1}(\theta_q)G_q(\theta_q)X + F_q^{-1}(\theta_q)DU \\ &= \overline{A}_q X + \overline{B}_q U \end{aligned} \tag{B.21}$$

where

$$\overline{A}_q = F_q^{-1}(\theta_q)G_q(\theta_q)$$

$$\overline{B}_q = F_q^{-1}(\theta_q)D$$

The discrete dynamic representation of Eq. (B21) is

$$X(k+1) = A_q(\theta_q)X(k) + B_q(\theta_q)U(k) \tag{B.22}$$

The derivation of discrete system matrices, $A_q(\theta_q)$ and $B_q(\theta_q)$, from continuous system matrices, $\overline{A}_q(\theta_q)$ and $\overline{B}_q(\theta_q)$, is given in reference [19].